GRAIN SHATTERING IN SHOCKS: THE INTERSTELLAR GRAIN SIZE DISTRIBUTION

A. P. JONES,[1,2] A. G. G. M. TIELENS,[2] AND D. J. HOLLENBACH[2]

ABSTRACT

We have studied the effects of shattering in grain-grain collisions. Based upon extensive numerical simulation of surface explosions and impacts, an analytical model has been developed which relates the final crater mass and fragment size distribution to the relative collision velocity, grain sizes, and material properties of projectile and target. Our model contains one free parameter, the critical shock pressure for shattering. We have compared the calculated crater masses to laboratory experiments on (sub)micron-sized particle impacts on a wide variety of materials and find good agreement assuming that the critical pressure for shattering is equal to the shear strength of the material. This critical pressure corresponds to minimum collision velocities of ~ 1 km s^{-1} for shattering to occur. The shattering threshold is much smaller than the vaporization threshold, and we therefore conclude that shattering dominates over vaporization in grain-grain collisions. The calculated size distribution of the shattered fragments scales with $a^{-3.3}$; slightly less steep than the Mathis, Rumpl, & Nordsieck (MRN) size distribution. Essentially, any shattering model where the size of the fragments is related to the pressure experienced will lead to fragment power-law size distributions with indices slightly steeper than ~ 3. The maximum fragment size increases with increasing crater size (i.e., increasing collision velocity) until the target grain is completely disrupted by the collision. For higher velocity collisions, our theory predicts that the maximum shattered fragment size will decrease again.

Dust destruction (return of grain mass to the gas) in the interstellar medium occurs predominantly in shock waves in the warm neutral/ionized medium (density $\simeq 0.25$ cm^{-3}, temperature $\simeq 10^4$ K). The new theory for grain shattering in grain-grain collisions has been incorporated into a grain destruction code and used to reevaluate the grain destruction rate in interstellar shocks in the warm medium. We find that, for all the grain materials we consider (graphite, silicate, silicon carbide, diamond, iron, and ice) nonthermal and thermal sputtering dominate the grain destruction. We also find that grain disruption (shattering) in grain-grain collisions dominates the grain mass redistribution.

We present detailed results for grain destruction as a function of the grain size and composition. In particular, we consider MRN size distributions of silicate and carbonaceous (amorphous carbon/graphite) grains. We also present results for silicon carbide, diamond, iron, and ice test particles. For both carbonaceous and silicate grains we find that the fractional destruction (i.e., return of solid material to the gas phase) is ≤ 0.5, for $v_s \leq 200$ km s^{-1}. The grain lifetimes against destruction, assuming the three-phase model of the interstellar medium, are 6×10^8 yr, and 4×10^8 yr, for carbonaceous and silicate grains, respectively, only slightly longer than previous studies that ignored shattering.

Grain shattering in grain-grain collisions in shock waves leads to the redistribution of the dust mass from large grains ($a \geq 1000$ Å) into small grains ($a < 500$ Å). After processing by a single shock, a major fraction of the grains larger than 300 Å have experienced shattering grain-grain collisions. The slope of the fragment size distribution produced in single collisions has little influence on the size distribution produced by shocks. Essentially, the resulting grain size distribution is slightly steeper than MRN, because the largest grains move at the highest postshock velocities and hence are preferentially shattered into the smallest fragments. Large grains are lost from the interstellar grain size distribution on time scales less than 10^8 yr in the warm medium. For 50 km s$^{-1} \leq v_s \leq 200$ km s^{-1} as much as 5%–15% of the initial grain mass (all grain radii ≥ 50 Å) may end up in sub-14 Å fragments. Thus, interstellar shocks may be a prodigious source of PAH molecules, PAH clusters, and small grains.

Given that the typical stardust injection time scale is 2.5×10^9 yr, we conclude that efficient mechanisms for grain growth, and in particular, the reformation of grains with radii ≥ 1000 Å, must exist in interstellar medium in order that the refractory elements be incorporated in dust and that most of the dust mass is in sizes ≥ 1000 Å, as observed.

Subject headings: dust, extinction — methods: numerical — shock waves — supernovae: general

1. INTRODUCTION

Interstellar dust is affected by the processes of grain growth, through accretion and coagulation in dense clouds, and grain destruction/disruption, through sputtering, vaporization, shattering, and disaggregation, in interstellar shocks (Bierman & Harwit 1980; Liffman & Clayton 1989; Seab & Shull 1983; Jones et al. 1994). Extinction measurements along diffuse and moderately dense lines of sight can be used, in conjunction with known optical parameters, to infer the size distribution of the dust in interstellar environments. The inferred dust size distribution has been described in terms of power-law size distributions (Mathis, Rumpl, & Nordsieck 1977, hereafter MRN), and binned size distributions (Kim, Martin, & Hendry 1994), which give

[1] Space Sciences Laboratory, University of California, Berkeley, CA 94720.
[2] NASA Ames Research Center, MS 245-3, Moffett Field, CA 94035.

good fits to the mean interstellar extinction curves. This interstellar dust size distribution is a balance between the formation and destruction processes that operate in circumstellar shells and in the interstellar medium. The observed extinction in the interstellar medium coupled with the depletions of the grain-forming elements (i.e., C, Mg, Fe, Si, O, etc.) and the strengths of the 10 μm and 20 μm SiO absorption features show that a large fraction of the heavy elements are locked up in dust (Mathis 1990). However, observations show that strong shocks can destroy dust (Routly & Spitzer 1952; Cowie 1978; Sembach & Savage 1996). Theoretical estimates of dust destruction in shocks indicate grain lifetimes of the order of $1-5 \times 10^8$ yr (Barlow 1978a, 1978b; Draine & Salpeter 1979a; 1979b; Dwek & Scalo 1980; Seab & Shull 1983; McKee et al. 1987; Jones et al. 1994). In contrast, the injection time scale of dust formed by red giants, supernovae, and novae is of order $\simeq 2.5 \times 10^9$ yr (Tielens 1990; Jones & Tielens 1994). Thus, grains must be shielded from destruction in shocks or must efficiently grow by accretion from the gas phase in dense interstellar clouds.

Grain shattering in grain-grain collisions is an important process because, in contrast to other processes, it leads to a redistribution of the grain mass through the fragmentation of large grains into small grains. As first pointed out by Biermann & Harwit (1980) in their study of the origin of the interstellar dust size spectrum, the MRN size distribution may be a natural consequence of the importance of shattering. More recently, Borkowski & Dwek (1995) have studied the fragmentation of dust in grain-grain collisions resulting from a size distribution of fast-moving dust particles decelerating in a dusty plasma. While their results are not directly applicable to interstellar shocks, they do show that the final dust size distribution exhibits an excess of small particles, compared to the initial size distribution. Liffman & Clayton (1989) have modeled the interstellar grain size distribution and chemical composition using ad hoc assumptions on the effects of shocks. However, to date, no detailed study of the microphysics of grain shattering and the effects of shattering on the grain size distribution in grain-grain collisions in interstellar shocks has been undertaken.

In this paper we have reconsidered the destruction and disruption of grains in interstellar shocks including the effects of grain shattering in grain-grain collisions using a new shattering theory that we present in § 2 of this paper. This is a detailed theory that allows us to determine the shattered mass, and the shattered fragment size distribution, in grain-grain collisions. As in our previous paper on grain destruction in shocks (Jones et al. 1994), we restrict our calculations to steady state shocks in the warm intercloud component of the three-phase model of the interstellar medium (McKee & Ostriker 1977), where grain destruction predominantly occurs. It is the destruction of the grains in the warm intercloud medium that determines the lifetimes of grains in the interstellar medium (see, e.g., McKee 1989; Jones et al. 1994).

In interstellar shock waves, grains undergo destructive and disruptive processing due to the relative grain-grain and gas-grain motions and to the random thermal velocities of the gas-phase species impacting on the grains. Differential grain velocities arise from the grain size and grain material density dependence of the postshock betatron acceleration and the gyro motion of the charged grains

around the magnetic field lines. Relative gas-grain velocities arise from the motion of the grains through the gas swept up by the shock, and from the thermal velocities of the gas atoms. The grains in our code are subjected to three destructive processes during their passage through a shock, namely, vaporization, nonthermal sputtering, and thermal sputtering, all of which return solid material to the gas phase. Vaporization is the atomization of all, or part, of a grain following impact with another grain. Sputtering arises from gas-grain impacts and leads to grain surface erosion through the removal of surface or near-surface species which may be atomic or polyatomic. The sputtering may be nonthermal, due to the motion of the grains with respect to the gas, or thermal, due to the thermal velocities of the gas-phase species with respect to the grains. We will refer to these three processes collectively as grain destruction. Grain-grain collisions can also lead to shattering: the fragmentation of all, or part, of a grain into smaller but distinct subgrains. We will call this process disruption. Hence, both destructive and disruptive processes can "move" a grain through the grain size distribution, but only the destruction processes can remove solid material from the grain size distribution and convert it to gas.

In this work we are primarily interested in the shock processing of amorphous carbon/graphite and silicate grains, but we also consider, as test particles, other possible interstellar, circumstellar, and dense cloud materials (e.g., silicon carbide, diamond, iron and ice). As in our previous work (Jones et al. 1994) we adopt the term "graphite" here for the amorphous carbon/graphite grains because we use the available graphite shattering, vaporization, and sputtering parameters to model the solid carbon component of interstellar dust. However, amorphous carbon has similar sputtering and vaporization properties (Tielens et al. 1994), and also similar shattering properties (this paper).

This paper is organized as follows: § 2 presents the grain shattering theory for grain-grain collisions, § 3 details the numerical method, § 4 describes the dynamics of grain-grain collisions in shocks, §§ 5 and 6 give the results of our calculations for MRN size distributions and test particles, §§ 7 and 8 discuss the grain lifetimes, large grain disruption timescales, and the formation of small grains, and § 9 presents our conclusions.

2. SHATTERING OF GRAINS

2.1. *Crater Formation*

Two phases can be discerned in the flow produced by the hypervelocity impact of a projectile on a target, the early-time and late-stage phases (e.g., Tielens et al. 1994). When a projectile impacts on a target at a high velocity, shock waves will propagate from the interface both into the target and into the projectile. When the shock wave reaches the back of the projectile, rarefaction waves will travel onto the shocked region relieving the high pressures. At the end of this early-time stage, the coupling of the projectile's energy and momentum to the target is essentially complete. In the second phase, the excavation stage, the shock has departed from the immediate vicinity of the projectile and the transient crater. There are now two separate flow fields in the target: the detached shock and the excavation flow (Bjork, Kreyenhagen, & Wagner 1967; Maxwell 1977; Orphal 1977; Trulio 1977). Figure 1 shows a schematic of the impact of a projectile on a slab.
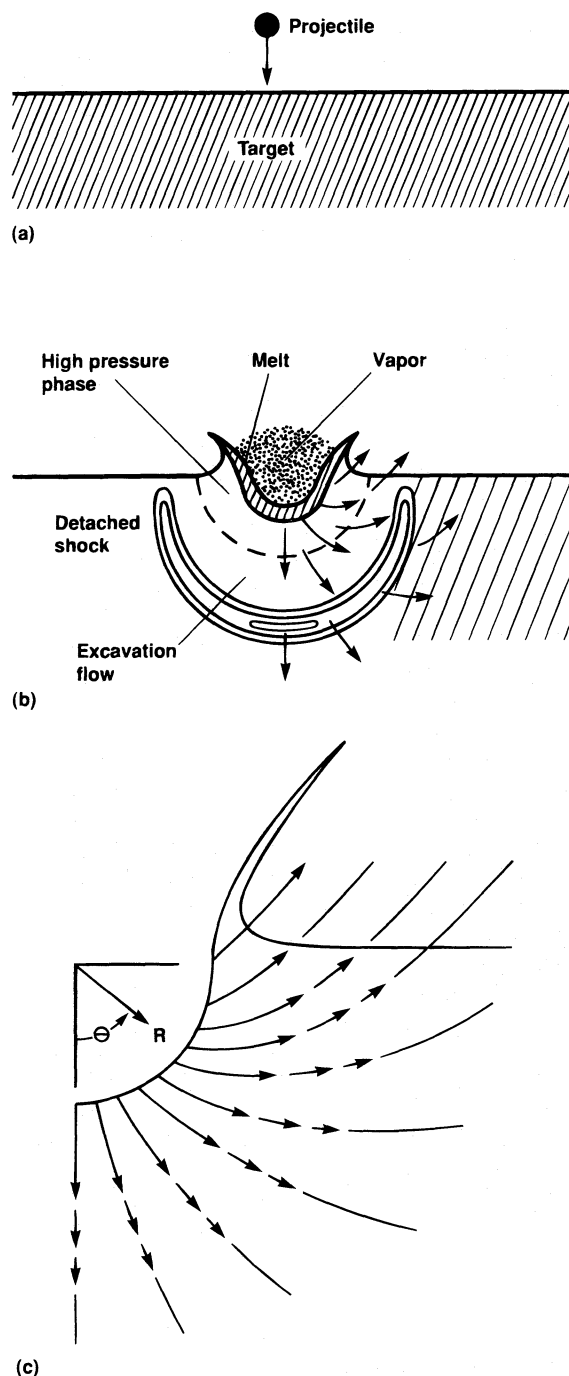
FIG. 1.—(a) High-velocity impact of a projectile drives a strong (detached) shock into the target. (b) This shock can lead to vaporization and melting of the target material. It will also create an excavation flow which carves out a crater. The arrows behind the shock indicate the velocity vectors associated with this excavation flow. (c) A schematic of the streamlines for the z model with z = 3. See text for details.

The hemispherical detached shock imparts a radially outward directed (i.e., into the target) velocity on the shocked material and the associated stresses are compressive. Although the dynamic pressure is high, shearing distortions are small and the detached shock has no direct influence on the cratering process. It can however, influence the cratering in an indirect way. In particular, for the pressures of relevance here (10^{11}–10^{13} dyn cm^{-2}), the (weak) shock wave will split into two separate waves (Zeldovich & Raizer 1966). First, an elastic wave will propagate into the

target, shocking it to the Hugoniot elastic limit (typically ~10^{10} dyn cm^{-2}). This shock wave will be followed by a plastic wave, which brings the material into the plastic state. This facilitates shearing motions.

Rarefaction waves propagating into the target from the free surfaces give rise to the excavation flow field. These rarefaction waves will unload the shocked material to zero pressure along an isentrope and accelerate the shocked material toward the free surface, which changes the character of the flow field significantly. Some of the initial internal energy of the shocked material is thereby converted into kinetic energy of the excavation flow. It is important to recognize that a solid requires smaller material displacements than a gas during unloading. Thus, while the transient crater cavity is still filled by a vapor at a relatively high pressure, the solid material close to the cavity surface will have relaxed to fairly low pressures (Trulio 1977). Consequently, the velocities imparted on the shocked material during unloading are not radially directed toward the crater cavity, but to the adjoining free surface (see Fig. 1). Directly below the impact site the motion is, of course, still directed inward, but along the transient crater walls the flow field has changed into a shearing flow along the walls. Even after the crater has achieved its maximum depth, excavation of the crater will continue in this shearing flow. Some of the material transported to the surface by this shearing flow will be ejected in the form of small fragments. The remainder may form a raised lip around the crater. Finally, for very high velocity impacts or large-projectile-to-target size ratios, complete destruction of the target may occur (catastrophic destruction).

In § 2.2, we will recapitulate our results (Tielens et al. 1994) for the propagation of the shock wave in solids and the implications for the cratering flow. Then, in 2.3, we will develop a simple model for the excavation flow which will relate the crater volume and shattered fragment size distribution to the material characteristics. Our results will then be compared and normalized to experimental studies on the craters produced by impacts of micron-sized particles in § 2.4. Catastrophic destruction of the target is discussed in § 2.5. Finally, the astrophysical implications for grain-grain collisions in interstellar shocks are examined in § 2.6.

2.2. Late Stage Equivalence

Unlike the detached shock, the location of the cratering flow region is quite stable. The upward accelerated material will flow along the transient crater wall until either its kinetic energy is dissipated by plastic work or until it is ejected. Assuming an elastic–perfectly plastic material,[3] the cratering flow will be purely hydrodynamic until strength effects become important; i.e., until the shear stresses in the cratering flow drop below the shear strength of the material. We can then use the concept of "late-stage equivalence" (Dienes & Walsh 1970; Kreyenhagen & Schuster 1977) to relate crater sizes to impact parameters such as velocity and mass of the projectile. Numerical and analytical hydrodynamical calculations show that the late-stage flow field for two impacts with the same $M_P v_r^\alpha$ are the same (where M_P is the projectile mass, v_r is the impact velocity, and α is a

---

[3] Elastic response below a critical pressure (i.e., a linear relation between stress and strain); plastic response (i.e., stress is independent of strain) above that pressure.

constant; Dienes & Walsh 1970; Kreyenhagen & Schuster 1977). Hence, impacts with identical values of this parameter will produce identical craters. We will base our analysis on the self-similar solution for shock wave propagation in solids developed in Tielens et al. (1994). A summary is presented here; more details can be found in Appendix A.

Consider the impact of a projectile with mass, M_P, and velocity, v_r, on a slab. In contrast to a spherically symmetric blast wave, the impact blast wave propagating into the target is characterized by a decrease of energy and an increase in momentum resulting from the hot vapor expanding into vacuum at the impact point. The mass of the target, M, shocked to a critical pressure P_1 is then given by (Tielens et al. 1994)

$$\frac{M}{M_P} = \frac{(1 + 2\mathscr{R})}{2(1 + \mathscr{R})^{16/9}} \frac{1}{\sigma_{1i}^{1/9}} \left(\frac{\mathscr{M}_r^2}{\sigma_1 \mathscr{M}_1^2} \right)^{8/9}, \qquad (1)$$

where $\mathscr{M}_r$ is the Mach number of the impact ($\equiv v_r/c_0$, with c_0 the target sound velocity), $\mathscr{M}_1$ is the Mach number corresponding to the critical pressure P_1, $\mathscr{R}$ is determined by material parameters, and σ depends on material parameters as well as the Mach number (see Appendix A). Since σ is nearly constant, the mass scales approximately with $P_1^{-8/9}$, slightly less steep than the constant energy solution, $V \propto P^{-1}$, due to the energy loss and momentum gain. As this relation illustrates, once the material and impact parameters have been specified, the cratering flow (i.e., the crater mass) is fully determined by one parameter: the critical pressure below which no further excavation occurs.

2.3. The Excavation Flow

Extensive studies of the cratering flow in numerical calculations of near surface explosions revealed surprisingly simple excavation flows (Maxwell 1973; Maxwell & Seifert 1976; Maxwell 1977; Orphal 1977). After the shock wave passage, the shocked material relaxes rapidly and the material density approaches its final, constant value. The excavation flow can thus be described as an incompressible flow. These studies have also shown that the flow is in steady state (i.e., flow velocity is independent of time at any spatial point) until strength effects become important. In spherical coordinates (see Fig. 1c), the radial velocity is given to a good approximation by

$$U_R = \frac{A_R}{R^z} \qquad (2)$$

with A_R and z constant. Using the incompressibility approximation, $\nabla \cdot U = 0$, the tangential velocity component is then given by

$$U_\theta = U_R(z - 2) \frac{\sin \theta}{1 + \cos \theta}. \qquad (3)$$

The particles move, thus, along streamlines which are defined by the condition that the instantaneous velocity is tangent at each point. These streamlines are given by

$$R = R_0 \left(\frac{1 - \cos \theta}{1 - \cos \theta_0} \right)^{1/(z-2)}, \qquad (4)$$

where R_0 and θ_0 refer to a point on a reference surface. When material strength effects become important the flow stops without appreciably changing direction (i.e., z is constant). The flow is thus characterized by two parameters,

the intensity parameter A_R and the shape parameter z. We note that $z < 2$ corresponds to downward directed flows, $z = 2$ to radial flows (i.e., spherical explosion in a infinite medium), and $z > 2$ to upward directed flows. For most of the analyzed numerical cases z is equal to about 3 (Maxwell 1977). Crater formation occurs on a time scale much longer than the loading time scale and thus represents a coasting process with zero total vertical momentum. The only z model flow which fulfils this condition is that for $z = 3$ (Maxwell & Seifert 1976). Our detailed analysis below will yield $z = 3.4$ for a projectile impacting on a target.

In the case of a projectile impacting on a target, the cratering flow is more complex than for near surface explosions described above (Austin, Thomsen & Ruhl 1981; Austin et al. 1981b). Essentially, in the impact case, the flow field center is moving down into the target with time during the early crater excavation stage due to the continued transfer of momentum from projectile to the target. Thus, although the flow is still incompressible and can be described well by the analytical z model at any time, during the early stages of the excavation flow, the flow is not in steady state and the streamlines are not the Lagrangian path of the particles. Nevertheless, comparison between numerical hydrodynamic calculations and the analytical z-model shows reasonable agreement for impact cratering (Thomsen et al 1979; Austin et al. 1981b). Hence, we will adopt the z model, because of its simplicity and because it contains the essential characteristics of crater formation—that is: incompressible, shearing flow along the crater walls. In principle, the center of origin for the excavation flow should be taken at a depth about equal to the projectile diameter (Thomsen et al. 1979; Austin et al. 1981b). However, anticipating that grain shattering will be dominated by small projectiles impacting at high velocities ($\simeq 100$ km s^{-1}) on a target grain, we will assume that this equivalent depth of burst is small compared to the final crater radius and thus can be neglected.

2.3.1. The Crater Volume

In our analysis, we will consider an elastic–perfectly plastic material; i.e., for small stresses, an increase in the (shear) strain will cause an increase in the (tangential) stress. When the stress exceeds a critical value (P_{cr}), the solid becomes plastic and an increase in the shear strain is no longer accompanied by an increase in the stress. Thus at that point the solid no longer resists any further increase in shear and will flow along the crater wall. The boundary of the crater is given by the condition that the pressure in the excavation flow has dropped to P_{cr}; from there on the material response will be elastic. This translates into the following condition on the flow velocity, $U(R_c)$,

$$U(R_c) = \frac{P_{cr}}{\rho_0 c_0}, \qquad (5)$$

where the particle velocity, U, refers to the excavation flow and not the detached shock, and ρ_0 is the material density. This simple expression gives a very similar result to a more detailed calculation (Bjork et al. 1967; Maxwell 1973; Maxwell & Seifert 1976) equating the kinetic energy of the excavation flow with the plastic work performed by it, assuming an elastic–perfectly plastic material. The crater radius is now given by

$$R_c(\theta) = \left\{ \frac{A_R \rho_0 c_0}{P_{cr}} \left[1 + (z - 2)^2 \frac{\sin^2 \theta}{(1 + \cos \theta)^2} \right]^{1/2} \right\}^{1/z}. \qquad (6)$$

The ratio of the diameter (D) to the depth (P) of the crater is then given by

$$\frac{D}{P} = 2[1 + (z - 2)^2]^{1/(2z)} \qquad (7)$$

which ranges from 2.0 to 2.5 for $z = 2$–4. The volume of the crater can be found from

$$V_c = 2\pi \int_0^{\pi/2} \int_0^{R_c(\theta)} r^2 \sin\theta \, d\theta \, dr \qquad (8)$$

which yields

$$V_c = \frac{2\pi}{3} \left[R_c\left(\frac{\pi}{2}\right) \right]^3 I(z) , \qquad (9)$$

where $I(z)$ is given by $I(z) = -8.53 + 13.04z - 6.42z^2 + 1.35z^3 - 0.10z^4$. For any z, the crater volume will scale as $(A_R/P_{cr})^{3/z}$. The streamline that passes through the crater radius, $R_c(\theta = \pi/2)$, marks the boundary of the ejected volume. That is, material above this streamline will be ejected while material below it will only be displaced leading to the formation of a lip (Croft 1980). The ejected volume, V_e, is given by

$$V_e = 2\pi \int_0^{\pi/2} \int_0^{R_e(\theta)} r^2 \sin\theta \, d\theta \, dr$$
$$= \frac{2\pi}{3} \frac{(z - 2)}{(z + 1)} \left[R_c\left(\frac{\pi}{2}\right) \right]^3 . \qquad (10)$$

Thus, for $3 < z < 4$, between 30% and 60% of the crater volume is ejected from the target.

2.3.2. The Size Distribution of the Ejected Particles

Material ejected at different distances from the impact point will be ejected at different velocities. The stresses associated with this velocity field will lead to break-up into small grains. The size, a_f, of the fragments ejected at a given radius from the crater center can then be evaluated by equating these stresses to the shear strength. The ejection velocity at a distance R, $U_e(R)$, is equal to

$$U_e(R) = U_R(R)[1 + (z - 2)^2]^{1/2} . \qquad (11)$$

Using equation (2), this corresponds to a velocity gradient

$$\frac{dU_e}{dR} = -z \frac{U_e(R)}{R} . \qquad (12)$$

Thus, the differential velocity, ΔU, across the grain diameter, $2a_f$, is then given by

$$\Delta U = 2za_f \frac{U_e(R)}{R} . \qquad (13)$$

Equating the stress, $\sigma = \rho_0 c_0 \Delta U$, to the critical stress leads after some rearrangements to

$$a_f = a_{f+} \left[\frac{R}{R_c(\pi/2)} \right]^{z+1} , \qquad (14)$$

where the maximum grain radius, a_{f+}, formed at the crater radius is given by

$$a_{f+} = \frac{R_c(\pi/2)}{2z} . \qquad (15)$$

The smallest size particles are formed at the inner radius, R_-, which is equal to the projectile radius for low-velocity impacts and to the vaporization radius, R_v, for high-velocity impacts. In the latter case, the minimum grain size is given by

$$a_{f-} = a_{f+} \left[\frac{R_v}{R_c(\pi/2)} \right]^{z+1} . \qquad (16)$$

We not that, for the size scales of interest, the energy associated with bond breaking required to create new surfaces is small compared to the kinetic energy of the ejected particles. The ratio of the kinetic energy, E_k, of an ejected particle to the energy required to create its surface, E_s, is equal to

$$\frac{E_k}{E_s} = \frac{\rho_0 a_f U_e^2}{6\gamma} = \frac{R^2 P_{cr}^2}{24 a_f z^2 \gamma \rho_0 c_0^2} , \qquad (17)$$

where γ is the surface energy per unit area. Anticipating our discussion in § 2.4, $P_{cr}/\gamma \simeq 3 \times 10^8$ cm^{-1}, $P_{cr}/\rho_0 c_0^2 \simeq 1$, and $R/a_f \gg 1$, we conclude that E_k/E_s is always much larger than unity. Hence, any shattering theory that equates the collision energy to the bond-breaking energy will produce too much surface area in the shattered fragments.

The volume, $dV(a_f)$, of a streamline ejecting particles with size a_f at a distance R_e can be found by integrating along a streamline

$$dV(a_f) = \int_{R_-}^{R_e} dA \, dS , \qquad (18)$$

where dA is the area of the streamline, dS the differential along it, and R_- the intersection with the inner boundary (i.e., vaporization boundary). Using incompressibility ($U \, dA = U_e \, dA_e$, where dA_e and U_e are the area and velocity at ejection) and $dS = U/U_R \, dR$ and assuming $R_e \gg R_-$, this yields

$$dV(a_f) = \frac{R_e}{z + 1} \frac{U_e}{U_R} dA_e . \qquad (19)$$

The volume of grains with size a_f in the interval (a_f, $a_f + da_f$) [i.e., ejected within (R_e, $R_e + dR_e$)] is equal to

$$dV(a_f) = \frac{z - 2}{z + 1} 2\pi R_e^2 \, dR_e . \qquad (20)$$

Defining $\tilde{a} = a_f/a_{f+}$, the number of grains, $n(\tilde{a})$, in a size interval $[\tilde{a}, \tilde{a} + d\tilde{a}]$ is given by

$$n(\tilde{a})d\tilde{a} = \frac{12z^3(z - 2)}{(z + 1)^2} \tilde{a}^{-\alpha_f} d\tilde{a} , \qquad (21)$$

where $\alpha_f = (4z + 1)/(z + 1)$. The exponent of this grain size distribution is not very sensitive to z; i.e., α_f varies only from 3.0 to 3.4 for z in the range 2–4. This is a very general conclusion. Any comminution process that leads to smaller sizes when the stresses involved increase will yield an exponent slightly steeper than 3. Essentially, this reflects the decrease of the average stress experienced when the volume increases (i.e., energy conservation).

2.3.3. Summary

The flow strength parameter A_R in the z-model for the excavation flow is proportional to $E_i^{z/3}$ where E_i is the kinetic energy in the impact (Maxwell 1977). Following our discussion on "late-stage equivalence" (§ 2.2; Tielens et al.

1994), this then implies that $z = 27/8$ ($=3.4$; see eq. [6]). For the size distribution of shattered fragments, we then find $n(\tilde{a})d\tilde{a} \simeq 34\tilde{a}^{-3.3} d\tilde{a}$. The maximum fragment size, a_{f+}, is $0.15R_c$. For a high-velocity impact, the minimum size is approximately given by (see eq. [16])

$$a_{f-} \simeq a_{f+}\left(\frac{P_{cr}}{P_v}\right)^{1.47}. \qquad (22)$$

Anticipating the discussion in § 2.4, $P_{cr}/P_v \simeq 0.1$ and the ratio of the minimum to the maximum size is about 0.03. For impacts at high velocity, where a major fraction of a large grain ($\simeq 3000$ Å) is shattered, the maximum and minimum sizes are 500 Å and 15 Å, respectively. However, for small projectiles impacting near the vaporization threshold, the minimum size is calculated to be less than that of an atom! The theory developed here is based upon continuum elastics and will break down when the strains become large (i.e., small size scales). At that point, bond breaking is more important than this theory assumes and P_{cr} should approach P_v. It is beyond the scope of this paper to develop a theory for the material response at such small size scales and, in our shock code, we will adopt 5 Å for a_{f-}, the minimum size in our grain size distribution.

2.4. Experimental Studies on Micrometeorite Impacts

Our theoretical results show that, apart from known material properties and impact parameters, the crater volume depends on the adopted value for the critical pressure. For macroscopic (ductile) bodies, measured tensile strengths of materials are typically 1 kbar (10^9 dyn cm^{-2}). This is much less than the ultimate tensile strength of a material ($\simeq G/6 \simeq 100$ kbar $= 10^{11}$ dyn cm^2, with G the shear modulus). This reflects the presence of imperfections, particularly line dislocations, which act as sources of mechanical weakness (Kittel 1976). Essentially, a crystal is highly strained near a dislocation and this promotes slip[4]. However, measured densities of dislocations are typically 10^{11} cm^{-2} corresponding to about one dislocation through a region with a diameter of 400 Å. Clearly, thus, movement of dislocations plays little role in crater formation of submicron-sized bodies and the critical pressure involved should approach the ultimate tensile strength of a material. As a corollary to this, macroscopic experiments on cratering by impacts will not provide a good benchmark for our theories of shattering of interstellar grains.

Over the years, extensive experimental studies of the impact of micron-sized particles on slabs of various materials have been performed because of the micrometeoroid hazards on interplanetary spacecraft, the interpretation of microcraters on lunar rocks, and the erosion of atmosphere-free planetary bodies (McDonnell, Flavill, & Carey 1976; Fechtig et al. 1977; Mandeville 1972; Vedder 1971; Rudolph 1969). Often these data are presented in terms of the ratio of crater volume to projectile energy averaged over a large number of impacts with different velocities. In a few cases, crater volumes have been presented for individual impacts. Figure 2 compares calculated ratios of the crater volume to the projectile kinetic energy to experimental data for impacts of iron projectiles on various metal-
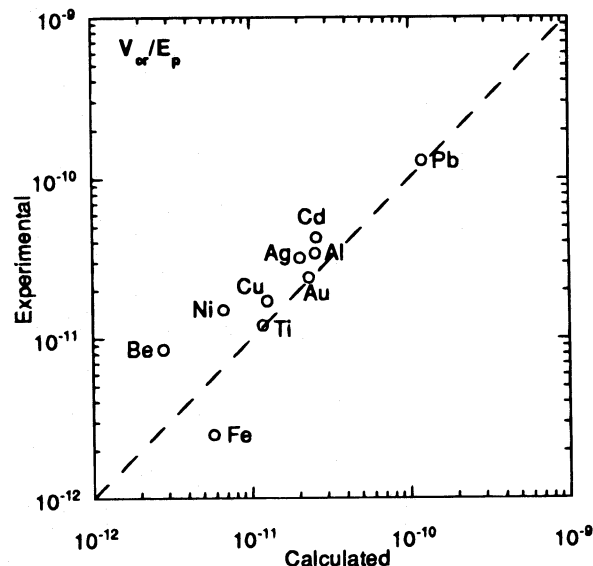

FIG. 2.—Average ratio of crater volume to kinetic energy (in units of cm^3 ergs^{-1}) for iron projectiles impacting various metallic surfaces. Calculated ratios have been evaluated using eq. (1) for a projectile velocity of 5 km s^{-1} and a critical pressure equal to the shear modulus of the target metal. The data, taken from the experiments of Rudolph (1969) and Fechtig et al. (1980), are generally averages over a range of velocities and masses. Typical collision parameters are micron-sized projectiles ($M_P \simeq 3$ pg) impacting at $\simeq 5$ km s^{-1}.

lic surfaces (Rudolph 1969; Fechtig, Nagel, & Pail 1980). Shock wave data have been taken from Marsh (1980). In all cases, the shear modulus was adopted for the critical pressure[5] in equation (1). The model results agree reasonably well with the data.

In Figure 3, we compare our model calculations for the ratio of crater to projectile volume as a function of impact velocity to experimental data for low-velocity impacts of iron projectiles on lead, aluminum, and copper surfaces (Rudolph 1969). For lead, good agreement is obtained for a critical pressure equal to the shear modulus. For aluminum and copper, we lowered the critical pressure slightly ($\simeq 25\%$) from the shear modulus in order to improve the fit. This shifts the calculated curves upward without affecting the slope noticeably. Our theory reproduces the measured dependence on impact velocity well. A similar comparison for the impact of micron-sized polystyrene spheres on soda-lime glass is shown in Figure 4. The latter impacts result in a small glass-lined pit surrounded by a larger spallation zone. The data plotted in Figure 4 refer to the spallation craters (Mandeville & Vedder 1971). The calculations have been made adopting a critical pressure of 300 kbars, a typical value for the shear modulus of glass. Again, the agreement between experiment and theory is reasonable. For 1 μm sized, aluminum and silica spheres impacting at 7 km s^{-1} on soda-lime glass slabs, the ratio of the crater volume to projectile kinetic energy is measured to be 8×10^{-12} cm^3 ergs^{-1} (Vedder 1976). For a critical pressure of 300 kbars, we calculate a value of 1.2×10^{-11} cm^3 ergs^{-1}, slightly larger than that measured. The crater diameter-to-depth ratio measured for impacts of micron-

---

[4] Macroscopic brittle bodies, such as glasses, fracture at low pressures (1 kbar) due to the presence of minute (submillimeter-sized) cracks which also act as stress enhancers.

[5] Following our discussion in § 2.3.3, this critical pressure refers to the pressure in the shock wave (P_1), not in the cratering flow (P_{cr}). The latter plays no direct role in our model calculations.
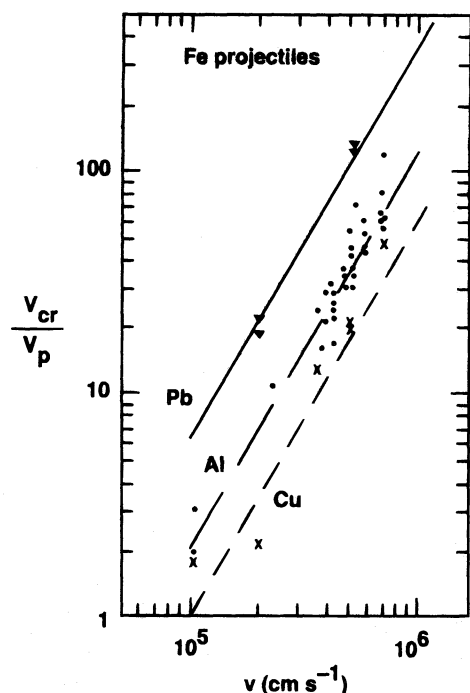
FIG. 3.—Ratio of the crater volume to projectile volume as a function of velocity for individual impacts of micron-sized iron projectiles. The data for lead (*filled triangles*), aluminum (*dots*), and copper (*crosses*) targets are taken from Rudolph (1969). The calculated ratios have been evaluated using critical pressures approximately equal to the shear modulus. See text for details.

sized projectiles on surfaces of the same material is about 2 (Nagel & Fechtig 1980), slightly lower than the value of 2.35 (for $z = 3.4$; see eq. [7]) predicted by our theoretical model.

Finally, we emphasize the existence of a threshold collision velocity below which colliding grains merely bounce without crater formation (Tielens 1989). This critical collision velocity corresponds to an initial shock pressure equal to the critical pressure of the target material. The existence of such a threshold velocity is well established experimentally (Vedder 1971; Mandeville & Vedder 1971). Measured values for impacts on glass range from 0.5 to 2 km s^{-1} depending on the projectile material, in good agreement
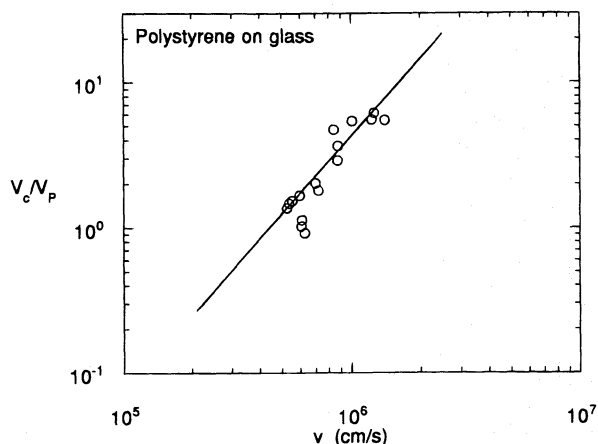

FIG. 4.—Ratio of the crater volume to projectile volume as a function of velocity for individual impacts of micron-sized polystyrene projectiles on soda-lime glass (Mandeville & Vedder 1971). The theoretical curve was calculated adopting a critical pressure of 300 kbars. See text for details.

with our calculated values. We conclude that material loss due to cratering in high-velocity impacts of submicron particles is well reproduced by our theoretical model with a critical (shock) pressure equal to the shear strength, G, of the target.

Very little information is available on the size distribution of the fragments produced by submicron impacts. McDonnell et al. (1976) have experimentally measured the size distribution resulting from micron-sized impacts at $\simeq 5$ km s^{-1} on a lunar sample. The exponent of their measured power law ($\simeq 3.5$) is in reasonable agreement with our theoretical estimate (3.3). However, scanning electron microscope (SEM) studies showed that the largest of their fragments, with sizes comparable to the crater radius, failed to get dislodged.

2.5. *Catastrophic Destruction*

The previous subsections dealt with shattering due to the cratering flow set up by the expanding shock wave. In this analysis, we essentially assumed an impact on a semi-infinite slab. However, since the cratering process is rather slow, the finite size of a target can influence the outcome of the shattering process when the shock wave breaks through the back of the target. In that case, the compressive shock wave is reflected as a tensile wave and failure under the tensile stresses (spalling) of the backside will occur when the tensile stress exceeds the tensile strength of the material (Rinehart & Pearson 1954)[6] If the shock is very strong, multiple spalls can occur and the whole grain will be fragmented by this spalling process rather than by the cratering flow. This process is sometimes called catastrophic destruction in the astronomical literature (see Dohnanyi 1978).

Somewhat arbitrarily, we will assume that catastrophic destruction dominates when half the target grain is shocked to the tensile strength, P_{cat}. For a given projectile-target combination, this corresponds to a critical spalling collision velocity, v_{cat}, given by

$$v_{cat} = c_0 \left[\frac{M_T}{(1 + 2\mathscr{R})M_P} \right]^{9/16} \sigma_1^{1/2} \sigma_{1i}^{1/16} (1 + \mathscr{R})\mathscr{M}_{cat} , \quad (23)$$

where M_T is the target mass, and $\mathscr{M}_{cat}$ is the critical Mach number corresponding to the tensile strength (see Appendix A). Analysis of the size distribution resulting from this spalling process is complicated by interference effects generated by multiple reflections at corners and edges which will result in enhanced stress levels at some locations. The resulting size distribution is thus somewhat sensitive to the shape of the particle and the impact geometry (see Fujiwara & Tsukamoto 1980). Here, we will make an estimate of the largest fragment size (i.e., disregarding these interference effects) and assume that the size distribution is given by equation (21), normalized to the total target mass.

The size scale of the largest fragment, a_{f+} is governed by the stress rate of the reflected tensile wave, dP/dr; viz.,

$$a_{f+} = \frac{P_{cat}}{dP/dr} . \quad (24)$$

---

[6] Spalling can also occur in the rarefaction wave propagating from the free surfaces adjoining the developing crater, particularly for brittle materials, such as glasses. Microcraters on such materials do show spallation zones. Since the crater size and maximum particle size are related to the tensile strength of the material, our analysis on the crater volume and fragment size distribution still holds, as borne out by a comparison between theory and experiments (see § 2.4).

The stress rate of the tensile wave reflects the rise time of the shock wave (Zeldovich & Raizer 1966). For our adopted Hugoniot equation, relating the shock and particle velocities (see Appendix A), the constitutive relation is given by (Bland 1964)

$$P = \rho_0 c_0^2 \eta + 2\rho_0 c_0^2 s\eta^2 , \quad (25)$$

where η is the strain given by

$$\eta = 1 - \frac{\rho_0}{\rho} = \frac{v_1}{c_0 + sv_1} . \quad (26)$$

As a result, the stress rate is given by

$$\dot{P} = \rho_0 c_0^2 \dot{\eta} + 4\rho_0 c_0^2 s\eta\dot{\eta} , \quad (27)$$

where $\dot{\eta}$ is the strain rate.

Now, the rise time of the shock wave will depend on the relationship between shear stress and strain rate; i.e., the viscosity. A number of studies exist of effective viscosities for shocks in solids (see Bushman et al. 1993; Swegle & Grady 1986). For many materials at low stresses ($<10^{11}$ dyn cm^{-2}), strain rates have been shown to scale as, $\dot{\eta} = A\sigma_{vis}^4$ with A a material-dependent constant (Swegle & Grady 1986). The viscous stress, σ_{vis}, is the difference between the stress on the Hugoniot and on the release isentrope. For the low pressures in the shock waves of these experiments, the viscous stress is only a small fraction of the total shock pressure and rises rapidly with shock pressure. However, at our high shock pressures, the viscous stress well exceeds the pressure on the release isentrope and this relation has to level off. The physical origin of this empirical relation between strain rate and stress is not well understood but it implies that the shock rise time is inversely proportional to the energy that is dissipated in the shock (Grady 1981). For these conditions, energy dissipation in shock waves results from the creation and development of dislocations. Typically 10% of the plastic work in a shock is transformed into the creation of dislocations (Horie 1980) until it reaches the saturation value of $\simeq 10^8$ ergs g^{-1} (Kittel 1976). This saturation energy corresponds to a shock pressure of 3×10^{10} dyn cm^{-2}, the bottom end of our range of interest. Hence,

we will assume that the critical density of dislocations has been reached. With this assumption, the pressure gradient is given by

$$\frac{dP}{dr} \propto \frac{P}{v_s} \propto v_1 \propto E_{kin}^{1/2} , \quad (28)$$

where E_{kin} is the kinetic energy of the impact. We will further assume that at the spalling threshold (i.e., $P = P_{cat}$), the maximum spall size is some fraction, f_{cat}, of the target size. The maximum spalling fragment size as a function of impact parameter is then given by

$$a_{f+} = f_{cat} a_T \left(\frac{v_{cat}}{v_r}\right) , \quad (29)$$

where v_{cat} is the impact velocity corresponding to the critical spall pressure and v_r is the relative collision velocity. Hence, the maximum grain size will decrease as the square root of kinetic energy of the impact. We will adopt $f_{cat} = \pi^{1/3}/2z \simeq 0.2$. For the critical shock pressure, we will adopt the shear modulus, G, of the material. Experimental studies on micron-sized impacts on brittle materials show a critical pressure for spalling (near the impact site) very much consistent with this assumption (Mandeville & Vedder 1971). These assumptions ensure a smooth transition in the grain-size distribution from the cratering flow domain to the spalling domain.

2.6. Astrophysical Implications

Table 1 summarizes material parameters relevant for the shattering of interstellar grains. As discussed in § 2.4, the experimental data show that the critical shock strength for shattering is equal to the shear modulus of the material. Typically, the critical grain-grain velocity at which cratering ensues, v_{crit}, is 1–10 km s^{-1}. Consistent with the relative ease with which graphite flakes, its critical velocity is at the low end of this range. Likewise, ice shatters readily. However, silicon carbide and diamond are rather robust materials which withstand shattering better than most other materials. In Table 1, we also compare the shattered and

TABLE 1
Shattering upon Grain-Grain Collision

| | Hugoniot[a] | | | | Shattering Threshold[b] | | | | |
Material	ρ_0 (g cm^{-3})	c_0 (km s^{-1})	s	P_v^c ($\times 10^{12}$) (dyn cm^{-2})	G^d ($\times 10^{12}$) (dyn cm^{-2})	v_{crit}^e (km s^{-1})	v_{cat}^f (km s^{-1})	$(M_v/M_{total})^g$	$(M_c/M_P)^h$
Silicate	3.3	5	1.2	5.4	0.3	2.7	175	0.023	455
Graphite/amorphous carbon	2.2	1.8	1.9	5.8	0.04	1.2	75	0.005	1925
SiC	3.1	7.7	1.1	8.6	1.7	8.8	565	0.12	55
Ice	1.0	2.0	1.4	0.09	0.03	1.8	115	0.25	820[i]
Iron	7.9	4.1	1.5	5.2	0.055	2.2	140	0.05	650
Diamond	3.2	7.8	1.4	5.8	5	16.1	1015	0.84	9[i]

[a] Hugoniot data taken from Marsh 1980.
[b] Shattering thresholds calculated for the impacts of like materials (i.e., $\mathcal{R} = 1$).
[c] Critical pressure for vaporization taken from Tielens et al. 1994.
[d] Critical shock pressure, P_{cr}, for shattering has been set equal to the shear modulus of the material.
[e] Critical velocity for the onset of crater formation.
[f] Catastrophic velocity to completely shatter the target grain calculated for the impact of a 50 Å projectile on a 1000 Å target.
[g] Ratio of the vaporized mass to the total mass affected (vaporized plus shattered) for the impact of a 50 Å projectile on a 1000 Å target at 50 km s^{-1}.
[h] Crater mass calculated for the impact of a 50 Å projectile on a 1000 Å target at 50 km s^{-1}.
[i] The vaporized mass, 80 and 9 M_P for ice and diamond, respectively, has been subtracted. For other materials, the vaporized mass is negligible at these collision parameters.

vaporized volumes. The vaporization thresholds have been adopted from Tielens et al. (1994). We find that the ratio of the vaporized mass, M_v, to total mass affected by the collision (vaporized plus shattered), M_{vs}, is well represented by $M_v/M_{vs} = 0.76(G/P_v)^{1.07}$, with P_v the critical vaporization pressure (Table 1). For graphite and silicates, this ratio is 0.005 and 0.023, respectively. Obviously, shattering will be the dominant process affecting the interstellar grain-size distribution.

Most of the shattered volume in interstellar shock waves results from high-velocity impacts of small projectiles on large targets. As an example, we consider a 100 km s^{-1} impact of a 50 Å grain on a 1000 Å target. The velocity at which catastrophic destruction of the target occurs, v_{cat}, is 75–600 km s^{-1} depending on the material parameters (Table 1). Obviously, graphite and ice are the most easily disrupted this way and SiC and diamond are the sturdiest. For a 100 Å impact, these catastrophic velocities are reduced to 23–175 km s^{-1}. Of course, a 1000 Å impact needs only the critical shattering velocity for complete disruption of the target.

Figure 5 illustrates the size distribution of shattered fragments that can be expected for the impact of graphite projectiles on 1000 Å graphite grains. At the critical velocity, the largest fragment size is somewhat smaller than the projectile size. As the impact velocity increases, the largest fragment increases as does the total crater volume. At the catastrophic velocity, the whole target grain is disrupted and the maximum fragment size is about one-fifth the target radius, independent of projectile size. Above the catastrophic velocity, the maximum size decreases with increasing velocity but the total volume shattered plus vaporized is constant. With increasing projectile size, the catastrophic velocity decreases. For the example shown in Figure 5, v_{cat} is about 75 km s^{-1} for $a_P = 50$ Å but decreases to 5 km s^{-1} for $a_P = 250$ Å. The total vaporized volume can become an important fraction of the total shattered volume for impacts of large projectiles. At the highest velocities considered in Figure 5, a 250 Å projectile impacting at 100 km s^{-1} vaporizes half the target volume. For smaller projectiles, the vaporized volume is negligible. The calculated fragment size distributions for different materials are compared in Figure 6. Like materials are assumed in these calculations. As expected from our discussion above, the total shattered volume is the largest for graphite and ice grains and smallest for SiC and diamond grains. Of course, the colliding ice grains have the smallest amount of kinetic energy and this should be kept in mind when interpreting these results. For all of these collisions, the collision velocity is below the catastrophic velocity and hence the maximum fragment size increases with the total crater volume.

We conclude that—in terms of total volume removed from a given grain size—shattering (disruption) dominates over vaporization. Of course, shattering only redistributes the grain volume over the grain sizes so that the lifetimes of interstellar grains (i.e., of total grain mass) are in first order affected only by gas-grain sputtering and vaporization and not by shattering. In second order, the redistribution of the total grain volume over the size distribution can affect the total grain lifetime, since smaller grains are generally less affected by destructive processes in interstellar shocks (Jones et al. 1994).

Recently, Borkowski & Dwek (1995) published a study of the effects of shattering on dust in grain-grain collisions.
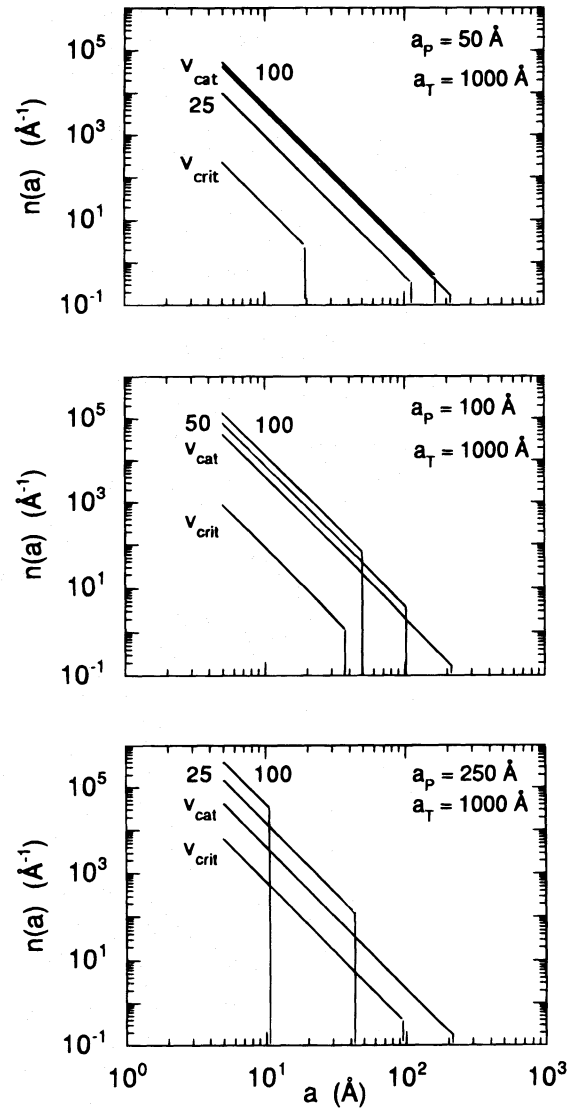
FIG. 5.—Calculated size distribution of shattered fragments as a function of projectile size and collision velocity. Projectile and target are graphite grains. The target size is 1000 Å. Projectile sizes are indicated in the panels. The curves are labeled by the collision velocity. The critical velocity is 1.2 km s^{-1} (Table 1). The catastrophic velocity is 75, 23, and 5 km s^{-1} for $a_P = 50$, 100, and 250 Å, respectively.
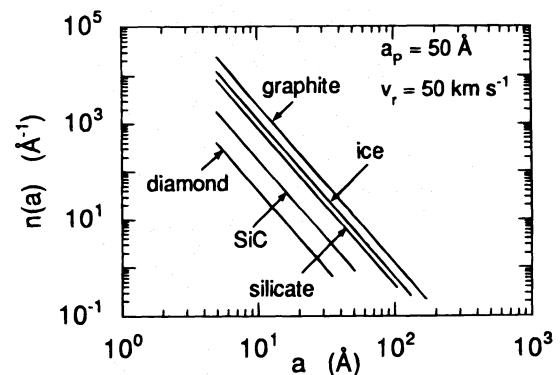
FIG. 6.—Calculated size distribution of shattered fragments for various grain materials for a 50 km s^{-1} impact of a 50 Å projectile on a 1000 Å target. Like materials have been assumed in these calculations. The results for iron grains are indistinguishable from those for silicates.

Their formalism is based upon a convenient parameterization of the crater mass and fragment size distribution but there is no link to the theoretical and experimental studies of shock waves in solids, the excavation flow, or crater formation. They rather arbitrarily assumed a critical energy for cratering of $0.3E_b$ with E_b the binding energy per atom. Inserting their value into equation (1), we find that they generally underestimate the crater volume by a factor 5 to 10 compared to our results. For silicates, the critical energy of 2 eV per atom adopted by Borkowski & Dwek (1995; $V_{cr}/E_P \sim 4 \times 10^{-12}$ cm^3 ergs^{-1}) is a factor of 2 less than our cratering model predicts ($V_{cr}/E_P = 10^{-11}$ cm^3 ergs^{-1})[7]. In particular, for graphite their critical energy is 1.8 eV per carbon atom which corresponds to $V_{cr}/E_P = 7 \times 10^{-12}$ cm^3 ergs^{-1}. Using the shear modulus (Table 1), we calculate $V_{cr}/E_P = 7 \times 10^{-11}$ cm^3 ergs^{-1}, an order of magnitude larger which reflects the ease with which the two-dimensional graphite structure flakes. They arbitrarily adopted a critical threshold for catastrophic disruption which is a factor of 3 less than for cratering (i.e., equivalent to $0.1E_b$ per atom). This is still a factor of 3 larger than our value for graphite but comparable to our value for silicates. As discussed above, our model agrees well with experimental data.

3. NUMERICAL SHOCK MODEL

We employ a theoretical model of shock structure and dynamics coupled with theoretical models of grain destruction in a numerical code to follow the time-dependent destruction of grains in shock waves. For a detailed description of the numerical method and basic model we refer the reader to previous papers (McKee et al. 1987; Tielens et al. 1994; Jones et al. 1994). In this new work, we have included the effects of grain shattering in grain-grain collisions and use the shattering scheme presented in § 2. This provides the distribution of the fragments resulting from shattering in a grain-grain collision as a function of grain-grain velocity and material parameters.

We assume an initial MRN power-law size distribution of spherical particles, where the grain number density per unit radius $dn_{gr}(a)/da$ is given, $dn_{gr}(a) = A_i n_H a^{-\alpha} da$ ($\alpha = 3.5$), with $A_{graphite} = 6.92 \times 10^{-26}$ cm$^{2.5}$ per H nucleus and $A_{silicate} = 7.76 \times 10^{-26}$ cm$^{2.5}$ per H nucleus for graphite and silicates, respectively (Draine & Lee 1984). The grains

are distributed across k_{max} logarithmically defined size bins for each grain material. The minimum and maximum initial grain radii are a_- (50 Å) and a_+ (2500 Å), and the upper size limit for a given kth bin is $a_+\delta^{k-1}$, where δ is the logarithmic size binning interval. In these calculations we have increased the number of bins, compared to our earlier work (Jones et al. 1994), in order to resolve the redistribution of the shattered fragments into small grains (radii <50 Å) during grain-grain collisions. We fixed the lower size bin limit to 5 Å, and then adjusted the width of the smallest size bin to include grains of radii 5–14 Å. For a logarithmic size binning interval of $\delta = 0.79$ (factor 2 in mass), for all but the smallest size bin, $k_{max} = 24$ covers grain radii from 2500 Å to 5 Å. The grains in all bins, except the final (24th), are subject to destructive and disruptive processing. We have chosen not to process these smallest fragments because they contain $\leq 10^3$ atoms, and the destruction and shattering schemes that we use are not appropriate for such small particles. The final bin is therefore merely a repository for the smallest grain fragments produced.

Based on the shattering scheme presented in § 2, we assume a shattered fragment size distribution power law of $\alpha_f = 3.3$ (slightly less steep than an MRN mass distribution power law of $\alpha = 3.5$). The maximum fragment dimensions possible can be calculated from equation (29) by setting $v_{cat} = v_r$. This yields $a_{f+} = 0.22a_T$, where a_{f+} is the maximum fragment radius and a_T is the target grain radius, in both the noncatastrophic and catastrophic collision cases. For the maximum grain size in the MRN distribution (2500 Å) this gives maximum graphite or silicate fragment radii of 540 Å. These are the maximum shattered fragment radii possible in any shattering collisions between any grains in a size distribution with a maximum radius of 2500 Å.

Again, in this work we use the fixed, radiative, steady state shock profiles (density, temperature, electron abundance, ionization structure, and photon flux as a function of the shocked column of gas) provided by Raymond (1992) and have considered the postshock grain destructive and disruptive processes as a function of the physical conditions as a parcel of gas and dust passes through these steady state profiles. We make no allowance for any grain destruction feedback into the shock (i.e., increased cooling due to an increased gas-phase abundance of the depleted elements), which is generally a reasonable assumption for the levels of grain destruction that we find (less than 50%). The relevant shock parameters are given in Table 2, and we (as in Jones et al. 1994) assume for our "standard" shock that $n_0 = 0.25$

---

[7] The values given are for relative velocities of 100 km s^{-1} and do have a slight dependence on velocity; see eq. (1).

TABLE 2

SHOCK PARAMETERS AND PRESHOCK CONDITIONS

NUMBER	$M_{A\perp}$	n_0 (cm^{-3})	B_0 (μG)	v_s (km s^{-1})	PRESHOCK IONIZATION STATE		UV FLUX G_0
					$n_{H^+}/n_{H(total)}$	$n_{He^+}/n_{He(total)}$	
1........	4.5	0.25	3	50	0.01	0.01	1.08
2........	9.0	0.25	3	100	0.50	0.25	1.77
3........	28.6	2.5	3	100	0.50	0.25	9.21
4........	90.4	25.0	3	100	0.50	0.25	86.99
5........	13.6	0.25	3	150	1.00	1.00	2.42
6........	18.1	0.25	3	200	1.00	1.00	3.51

NOTE.—$M_{A\perp}$ is the Alfvén Mach number perpendicular to the velocity vector. The UV photon flux term, G_0 (McKee et al. 1987, eq. [5.9]), is the total flux (shock-generated plus interstellar) normalized to that of the interstellar radiation field; i.e., $G_0 = 1 + (F_{UV,shock}/F_{UV,IS})$, where $F_{UV,shock}$ and $F_{UV,IS}$ are the shock-generated and interstellar UV fluxes.

cm^{-3}, $n_e = 0.13$ cm^{-3}, $v_s = 100$ km s^{-1}, and $B_0 = 3$ μG (shock 2 in Table 2, representative of supernova shocks in the warm diffuse phase of the interstellar medium). In these calculations, we have assumed cosmic elemental abundances of H, He, O, C, N, Ne, Fe, Si, Mg, and S (Allen 1983). The fractions of the refractory elements assumed to be in dust are O (0.16), C (0.58), Fe (0.95), Si (0.90), and Mg (0.95) (Draine & Lee 1984); all other elements are assumed undepleted.

We have subjected the new shattering portion of our code, and its integration into the previous code, to a series of tests to check for mass conservation and the accuracy of the results. The grain shattering code was rigorously tested for mass conservation through our standard shock, by ensuring that all the shattered fragments lie within the defined mass limits, i.e., all fragment radii ≥ 5 Å. In these tests shattering was considered in isolation from the destructive processes, by switching off the destruction schemes. The results of these shattering-only tests indicate that the total grain mass is conserved to better than one part in 10 million for two-component (graphite and silicate) size distributions.

4. GRAIN-GRAIN COLLISION DYNAMICS

In our previous work (Jones et al. 1994) we showed that the grain-grain collisional destruction process of vaporization only dominates over sputtering for shock velocities $\lesssim 50$–80 km s^{-1}, and then only for the largest of the grains in the size distribution. For vaporization-only collisions, the most destructive collision partners for the large grains ($a > 1000$ Å) are collisions with other large grains. However, these collision events are rare in a shock due to the low abundance of large grains. Collisions with the smallest grains in the size distribution ($a \sim 50$ Å) have the highest probability, and a large grain will experience many such collisions per shock. However, these collisions are less destructive due to the low mass of the smaller "projectile" grains, and the fact that only a small fraction of the target grain's mass is shocked to the vaporization limit. Thus, although a large grain may see many such collisions per shock its mass will not be greatly reduced by these collisions.

The inclusion of shattering into the grain processing has profound effects upon the outcome of the grain-grain collisions because the threshold pressures for this process are more than an order of magnitude smaller than those for vaporization (see Table 1 and Jones et al. 1994). Thus, shattering in grain-grain collisions leads to a massive disruption of the target grain for much lower projectile energies than for vaporization. In effect, one collision (for example, a 50 Å projectile on a 1000 Å target at ~ 100 km s^{-1}) is generally sufficient to completely disrupt a large grain through shattering. We examine the vaporization and shattering collision dynamics in more detail in the following sections.

4.1. Destructive Potential; Vaporization versus Shattering

In order to estimate the most destructive grain-grain collisions for large interstellar grains, we consider here a simple model in which a large target grain of radius a_T travels at a constant velocity v_T through a cloud of stationary projectile grains. This simple model provides a good representation of the destructive potential of grains in shocks because small grains ($a < 100$ Å) in a shock are at rest with respect to the gas by the time large grains have reached their maximum

velocities. This simple treatment, which does not correctly take into account the relative velocity for collisions between large grains in shocks, nevertheless gives some useful insights into the grain-grain collision dynamics.

The cloud of stationary projectile particles is assumed to have a MRN power-law size distribution, i.e., $dn_P(a_P) = A_i n_H a_P^{-3.5} da_P$, where a_P is the projectile radius. The sum of the large grain destruction rate (vaporization) and the disruption rate (shattering), expressed in terms of volume, is given by

$$\frac{1}{n_H} \frac{dV_T}{dt} = v_T \frac{4}{3} \pi a_T^3 A_i \int_{a-}^{a+} \sigma_{TP} a_P^{-3.5} f_j \, da_P \,, \qquad (30)$$

where σ_{TP} is the target-projectile collision cross section, and f_j is the fraction of the target grain destroyed by vaporization and disrupted by shattering determined using the appropriate material parameters given in Table 1 and by Jones et al. (1994). The parameter f_j is the sum of the vaporized and shattered fractions, i.e., $f_j = (f_{vap} + f_{sh})$ with the limitations that $f_j \leq 1$ and vaporization always takes precedence over shattering [$f_{sh} \leq (1 - f_{vap})$, see Appendix B].

Figure 7 shows the target grain destruction and disruption rates expressed as volume fraction destroyed per year per unit hydrogen nucleus density as a function of the projectile radius for graphite projectile and target particles, with $a_T = 2500$ Å. Initially, the shattering and vaporization rate increase slowly ($\propto a_P^{0.5}$) with projectile size, reflecting the increased target volume affected by the process ($f_j \propto a_P^3$) convolved with the decreased projectile abundance [$n_P da_P \propto a_P^{-2.5} d \ln (a_P)$, in log bins]. Eventually, the whole grain is shattered or vaporized by the collision and these rates reach a maximum. For shattering the maxima occur at ≈ 100 Å for $v_T = 50$ km s^{-1} and at ≈ 80 Å for $v_T = 100$ km s^{-1}, and for vaporization the maxima occur at ≈ 1000 Å for $v_T = 50$ km s^{-1} and at ≈ 550 Å for $v_T = 100$ km s^{-1}. Hence, for vaporization the most destructive projectiles have radii about an order of magnitude larger (i.e., projectile mass $m_p \approx 10^3$ larger) than the most disruptive projectiles, i.e., those that cause shattering. For larger projectile radii the vaporization rates decrease because of the decline in abundance of the projectiles with size. For vaporizing collisions, $f_j \sim 1$, $n_P \propto a_P^{-2.5}$, $\sigma_{TP} \propto (a_P + a_T)^2$, and the
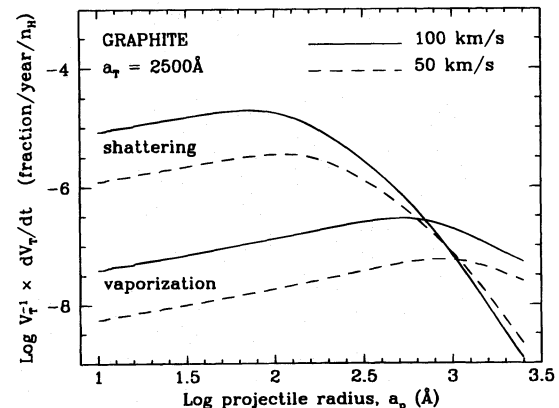
FIG. 7.—Fractional destruction and disruption rate for 2500 Å target grains traversing a cloud of stationary projectile grains, all grains are graphite. The destruction and disruption rate is shown for vaporization and shattering for two target grain velocities (50 km s^{-1} and 100 km s^{-1}). Note that we do not include sputtering in these calculations.

destruction rate is $\propto a_P^{-1.5}$ (in log bins) because $dV_T/dt \propto a_P^{-2.5}(a_P + a_T)^2$ and the $2a_P^{-1.5}a_T$ term dominates. For shattering, as the projectile radius increases the disruption rate is $\propto a_P^{-2.5}$ (i.e., it just depends on the projectile abundance because for the shattering maxima $a_P \ll a_T$, and σ_{TP} is essentially constant) but then decreases rapidly with a_P because a larger fraction of the target is vaporized. Finally, we emphasize that the shattering of large grains by small projectiles is more than two orders of magnitude more important than vaporization (Fig. 7). Thus, we again conclude that shattering will dominate over vaporization in grain-grain collisions in shock waves in the interstellar medium.

4.2. *Shattered Fragment Velocities*

Here we perform calculations for the post-injection velocities of the fragments produced by shattering in grain-grain collisions. In order to calculate the velocities of grains of radius a_k we adopt the scheme of McKee et al. (1987), where the acceleration of these grains is given by

$$\frac{dv_k}{dt} = \frac{d\chi}{dt}\frac{v_k}{2\chi} - \frac{F_D(\text{collision}) + F_D(\text{plasma})}{(4/3)\pi a_k^3 \rho}, \quad (31)$$

where v_k is the velocity of the grains, of density ρ, in the kth size bin, χ is the compression behind the shock, $F_D(\text{collision})$ and $F_D(\text{plasma})$ are the collisional and plasma drag terms. The first term on the right-hand side of equation (31) is the betatron acceleration term.

The shattering process injects new small grains into the postshock gas with velocities different from those of the unshattered grains of these radii. In particular, small grains are typically at rest at the postshock position where large grain shattering occurs. The small fragments produced by shattering will be quickly brought to rest with respect to the gas by collisional and plasma drag, but some further destruction and disruption may take place during this slowing down process (Borkowski & Dwek 1995). We have therefore performed test particle calculations in order to calculate the post-injection destruction for a range of fragment radii as a function of the shocked column (§ 4.3). For further details of the test particle calculations, see § 6. The velocities are calculated numerically using equation (31) in order to follow the fragment trajectories through the postshock gas.

It is also possible to analytically calculate the fragment post-injection velocities if we ignore the betatron acceleration of the fragments, which is generally small by the time that most shattering occurs, and second, if we ignore plasma drag, which is only important at low velocities where no sputtering destruction occurs. With these assumptions equation (31) reduces to

$$\frac{dv_k}{dt} = -\frac{F_D(\text{collision})}{(4/3)\pi a_k^3 \rho}. \quad (32)$$

The collisional drag term $F_D(\text{collision})$, taken from equation (3.9) of McKee et al. (1987) is

$$F_D(\text{collision}) = \pi a_k^2 v_k \rho_{\text{gas}}\left(v_k^2 + \frac{128kT}{9\pi\mu_H}\right)^{1/2}, \quad (33)$$

where $\rho_{\text{gas}} = \mu_H n_H$ is the mean gas density, and $\mu_H = 1.4 m_H$ is the mean atomic mass of the gas. For the velocities of interest the second term in parentheses is always $\ll v_k^2$, and

the fragment post-injection deceleration is therefore

$$\frac{dv_k}{dt} = -\frac{1.05 m_H n_H}{a_k \rho} v_k^2. \quad (34)$$

Solving equation (34) for the fragment velocity as a function of the shocked column of gas we find

$$v_k[N_H(t)] = \frac{v_0}{1 + 1.05(v_0/v_s)(n_H/n_0)(m_H/a_k \rho)[N_H(t) - N_H(0)]}. \quad (35)$$

The zero subscripts in the above equation indicate the preshock density (n_0), the fragment injection velocity (v_0), and postshock column density at injection [$N_H(0)$]. This analytical expression for the post-injection fragment velocities agrees well with the results for our numerical calculations. In these numerical and analytical calculations we injected test fragments with radii ranging 25–500 Å into our standard 100 km s^{-1} shock at an initial injection velocity of 100 km s^{-1} at a shocked column of $N_H = 10^{17.5}$ cm^{-2}. This gives a good simulation of the injection of shattered fragments at the peak velocity of the largest grains, where the shattering disruption is a maximum (see § 5). Figure 8 shows the post-injection velocities for a range of graphite fragment radii calculated numerically using equation (31) in our shock code, and also the velocities for the same fragments calculated using the analytical expression given in equation (35). The analytical velocity values values decay somewhat more slowly than the numerical values because the effects of plasma drag have been ignored in the analytical velocity calculations. We find that the analytical expressions gives a good fit to the numerically calculated velocities above the sputtering threshold. Below this threshold only grain-grain collisions can occur, but as we will show below (§ 4.3), these can be neglected. As expected, the fragments are slowed down in a column much less than the total shock column.

4.3. *Fragment Destruction and Disruption*

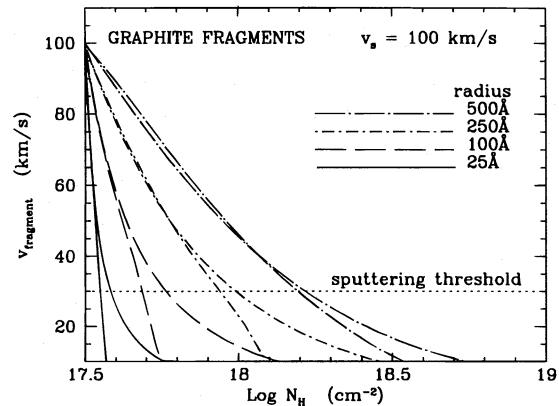In this section, we will estimate the further destruction and disruption of fragments produced by a shattering grain-

FIG. 8.—Test particle velocity calculations for graphite shattered fragments injected into a 100 km s^{-1} shock at 100 km s^{-1} and a column density of $10^{17.5}$ cm^{-2}. Numerical and analytical values are presented, the numerically calculated velocities are those that decay more quickly due to the inclusion of plasma drag in the calculation. The sputtering threshold velocity is also indicated.

grain collision in a shock. We will do this in an iterative manner. First, the destruction and disruption of the interstellar grain population is calculated without considering the slowing destruction and disruption of the slowing grain fragments in the shock (first-order); i.e., after their formation, the fragments are simply placed in the appropriate bin, at the velocity of the particles in that bin, where they undergo the same processing as all other grains in that bin. Second, we will study the further shock processing of the grain fragments by treating them as test particles and then take into account the destruction and disruption of all fragments during slowing in the shock (second-order). In the second-order calculation the fragments are affected by thermal and nonthermal sputtering and by collisions with grains in the shock (the grain size distribution derived from the first-order calculation) during their slowing to the velocity appropriate for their size. However, we assume that processing of the fragments during this slowing does not affect the processing of other particles in the shock. We will concentrate here on fragments injected into the shock at the shocked column density equivalent to the maximum in the postshock velocity for the largest grains. This is the point in the shock at which the shattering destruction peaks and therefore gives a good estimate for the further processing of shattered fragments. The velocity profile of the fragments is given by the results of § 4.2 (shown in Fig. 8).

In Figure 9 we present the cumulative number of collisions of fragments with all grains in the shock for the standard 100 km s^{-1} shock. In calculating the total number of collisions of the fragments we have assumed that the fragments undergo no destruction during slowing, i.e., we have calculated the total number of collisions for the fragment velocities shown in Figure 8. The results of these test calculations show that fragments with radii ≤ 200 Å undergo less than one collision with another grain during slowing down. The destruction of the sub-200 Å fragments is dominated by (nonthermal) sputtering. Larger fragments (radii > 200 Å) see at most a few tens of collisions during slowing. These collisions are predominantly with small particles (radii ≤ 15 Å), occur at relative velocities ≤ 50 km s^{-1} (see Fig. 8 and 9), and are cumulatively sufficient to disrupt most of the shattered fragments with radii greater than 200 Å. However, the larger fragments, with radii 200–500 Å, make up only a small fraction (≤ 0.05) of the total shattered mass of all the fragments (radii 5–500 Å), i.e., $\geq 95\%$ of the shattered fragments are smaller than 200 Å.

In Figure 10 we show the initial MRN size distribution and the first-order and second-order calculation final size distributions after processing in a 100 km s^{-1} shock, for grain radii from 30 Å to 400 Å; outside this size range little difference in the distributions is discernible. In the first-order calculation we make no allowance for fragment destruction and disruption during slowing, but in the second-order calculation the fragments have been subjected to all destructive and disruptive processes during slowing, including secondary fragmentation of the fragments larger than 200 Å. This figure shows that the first-order calculation overestimates the final grain abundances for grain radii 200–300 Å, and that this overabundance is about 25% for grain radii ≈ 230–280 Å. The effects of fragment destruction and disruption during fragment slowing are limited to a small range of grain radii and are predominantly due to the secondary fragmentation of the largest shattered fragments. Thus we can ignore the effects of secondary fragmentation in our calculations without significantly affecting our results.

Therefore, in determining the processing that the fragments undergo during slowing, we consider only nonthermal sputtering and neglect the shattering and vaporization effects of fragment-grain collisions. In their study, Borkowski & Dwek (1995) conclude that, except for very large fragments (radii > 0.2 μm) at high velocities ($v > 200$ km s^{-1}), secondary fragmentation can be ignored in their model of dust particles decelerating in a dusty plasma. As emphasized earlier our largest fragment is ~500 Å, considerably less than 0.2 μm (§ 3).
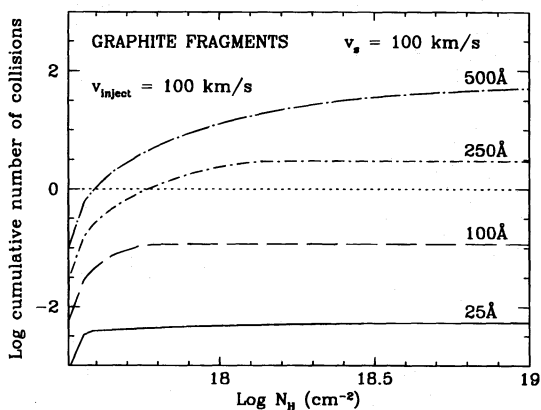

FIG. 9.—Cumulative number of collisions, i.e., the total number of collisions with grains that a fragment sees during slowing, for the test fragment velocities shown in Fig. 8.
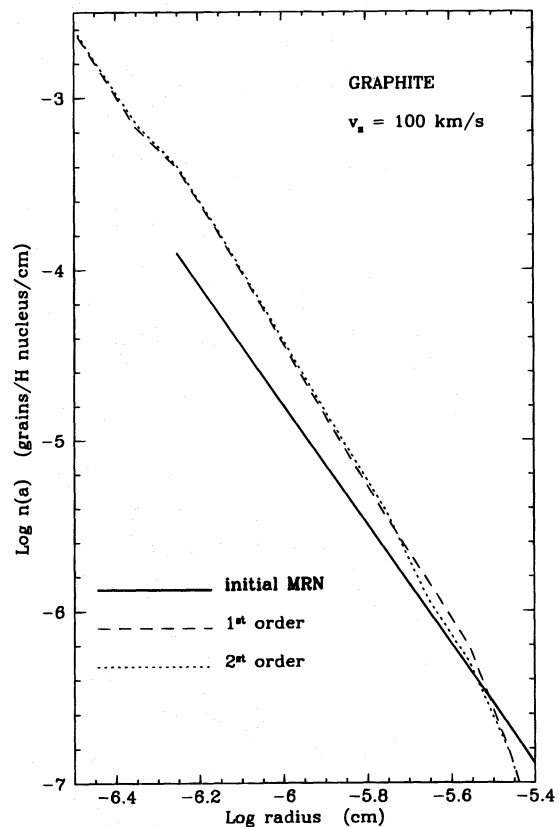

FIG. 10.—Graphite grain initial MRN (solid) and postshock size distributions for first-order (dashed) and second-order (dotted) shattered mass redistribution schemes, for $v_s = 100$ km s^{-1}. See text for full explanation.

4.4. *Shattered Fragment Destruction Scheme*

Given the result from the previous section, we will neglect the effects of grain-grain collisions on the slowing fragments. We then need consider only nonthermal sputtering during the slowing of the fragments. For a grain of radius a_{gr}, and density ρ, moving at velocity v_{gr} with respect to the gas, the sputtered volume, V_{sp}, in a time t is given by

$$V_{sp} = \int_0^t \frac{\pi a_{gr}^2 \, n_H \, v_{gr} \, Y_{sp}(v_{gr}) \mu_{sp}}{\rho} \, dt' , \qquad (36)$$

where $Y_{sp}(v_{gr})$ is the sputtering yield integrated over all gas phase atoms, and μ_{sp} is the mass of the species (atom or molecule) sputtered from the grain surface. Combining equations (34) and (36), and dividing by the grain volume, we obtain an expression for the fraction of the volume lost due to sputtering, V_{sp}/V, during the slowing of a fragment, i.e.,

$$\frac{V_{sp}}{V} = 0.71 \mu_{sp} \int_0^{v_0} \frac{Y_{sp}(v_{gr})}{v_{gr}} \, dv_{gr} , \qquad (37)$$

where μ_{sp} is mean atomic mass of the sputtered species in amu. Note that the fraction sputtered during slowing is independent of the initial particle size, i.e., all fragments lose the same fraction of their volume to the gas through sputtering. Hence, we have to perform only the integration in equation (37) once for each grain material for a series of injection velocities v_0. Figure 11 shows V_{sp}/V as a function of the fragment injection velocity for six grain materials. We have fitted the fragment sputtering curves with third-order

polynomials

$$\frac{V_{sp}}{V} = \sum_{i=0}^3 b_i v_0^i , \qquad (38)$$

where the fragment injection velocity, v_0, is in units of km s^{-1}. Table 3 lists the coefficients b_i and those polynomials are accurate to 3% in the range 30–150 km s^{-1}.

In our code the fragment radii are reduced by the amount sputtered during the slowing of the fragment, and the remaining fragment of radius a_f(slowed) is then put in the appropriate size bin $a_k \leq a_f$(slowed) $\leq a_{k+1}$. The remaining fragment, a_f(slowed), is given by

$$a_f(\text{slowed}) = \left[1 - \frac{V_{sp}}{V}(v_0) \right]^{1/3} a_f(v_0) , \qquad (39)$$

where $a_f(v_0)$ is the fragment radius before sputtering. Thus we allow for the mass loss from the fragments by sputtering during slowing without the need to follow each generation of shattered fragments throughout their mass-velocity space in the postshock gas. This considerably simplifies the numerical scheme, since a given grain has a fixed velocity at any point in the shock, and makes for shorter computation times. Borkowski & Dwek (1995) have adopted a more rigorous approach in their studies of grain shattering during slow down, but from our analysis above the two methods will yield the same results.

Although we have here considered only the effects of nonthermal sputtering during slowing, by virtue of the fact that a grain fragment is always present in some bin we also account for the thermal sputtering that occurs to that grain.

To summarize our algorithm: we calculate the shattered fragment size spectrum from a parent grain, modify that spectrum to include the effect of nonthermal sputtering as the fragments slow from the parent grain velocity to the velocity appropriate to the small fragment size, and instantaneously put them in the appropriate mass bin. The fragments then evolve along with the other particles in that bin (some previously shattered fragments, some original preshock grains).

5. RESULTS AND DISCUSSION

We have calculated graphite and silicate grain destruction and disruption for a range of shocks, including shock velocities v_s of 50, 100, 150, and 200 km s^{-1} and a range of preshock densities ($n_0 = 0.25$, 2.5, and 25 cm^{-3}). The shock parameters are given in Table 2 and the results of these calculations for grain destruction (dust returned to the gas) are presented in Table 4. The inclusion of shattering in
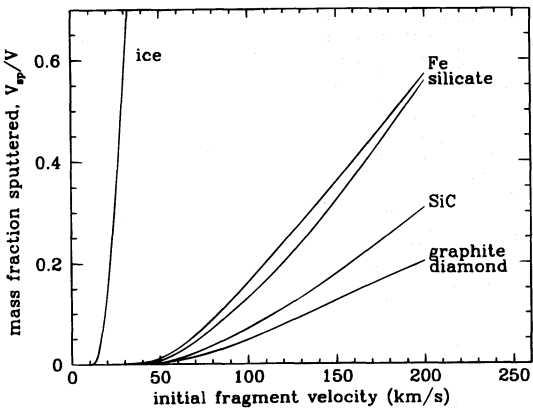

FIG. 11.—Mass fraction sputtered from fragments as a function of the initial injection velocity.

TABLE 3
FRAGMENT SLOWING SPUTTERING FITS (30–150 km s^{-1})

Material	b_0	b_1	b_2	b_3
Graphite/amorphous carbon	0.02376	$-0.13233E-2$	$0.20262E-4$	$-0.45939E-7$
Silicate	0.07107	$-0.40067E-2$	$0.62749E-4$	$-0.16570E-6$
Silicon carbide	0.04702	$-0.25023E-2$	$0.37207E-4$	$-0.97758E-7$
Diamond	0.02376	$-0.13233E-2$	$0.20262E-4$	$-0.45939E-7$
Iron	0.08251	$-0.47683E-2$	$0.78764E-4$	$-0.23121E-6$
Ice	0.28100	-0.05186	$0.25260E-2$	$-0.14933E-4$

$$(V_{sp}/V) = \sum_{i=0}^3 b_i v_0^i \; (v_0 \text{ in km s}^{-1})$$

TABLE 4

PERCENTAGE GRAPHITE/SILICATE DESTRUCTION (by mass)

	v_s (km s^{-1})			
MODEL	50	100	150	200
$n_0 = 0.25$ cm^{-3}	1.1/1.7	7.0/18.4	12.4/31.6	46.7/49.0
$n_0 = 2.5$ cm^{-3}	...	10.8/30.7	...	...
$n_0 = 25$ cm^{-3}	...	12.5/36.9	...	...

NOTE.—All models assume $B_0 = 3$ μG.

grain-grain collisions dramatically affects the evolution of large grains in shock waves and leads to the formation of large quantities of small grains. In this section we describe our results in detail and make some comparisons with our previous work in which the grain-grain collisions were vaporizing-only (Jones et al. 1994).

In Figure 12 we show the shock structure (temperature, $T_4 = T/10^4$ K, density, n_0, and electron abundance, x_e) for a "standard" 100 km s^{-1} shock with Alfvén Mach number, $M_{A\perp} = 9.0$, corresponding to $n_0 = 0.25$ cm^{-3} and $B_0 = 3$ μG. Also shown in this figure are the graphite grain velocities for three representative grain radii. The two phases of postshock grain betatron acceleration, associated with the cooling of the gas, are clear in the velocity data, one just behind the shock front, $N_H = 10^{14}$–10^{15} cm^{-2}, where the gas is rapidly ionized, and a second, $N_H = 10^{16.25}$–$10^{17.5}$ cm^{-2}, just prior to the recombination of the gas at $T = 10^4$ K. The grain velocities are particularly important because the degree of grain destruction and disruption is primarily determined by the relative gas-grain and grain-grain velocities. The flow time for the shock is given by $t = N_H/n_0 v_s = 10^{3.5}(n_0/1$ cm$^{-3})^{-1}(N_H/10^{18}$ cm$^{-2})$ yr, and a grain spends $\sim 10^5$ yr in the warm ($T_k > 100$ K) regions of the shock. In Figure 12 columm density can be converted to time using $\log t(\text{yr}) = \log N_H - 13.90$.
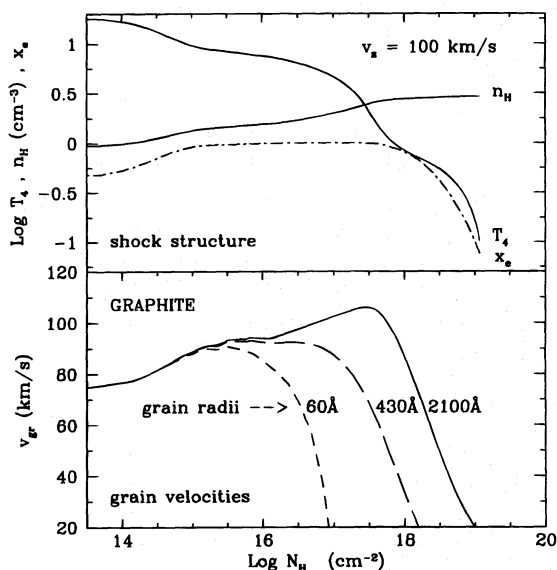
In Figures 13a, 13b, and 13c we show the graphite grain evolution, for the "standard" shock, plotted in a variety of ways. Figure 13a shows the destruction rate expressed as fraction destroyed per year for vaporization and sputtering destruction process. The disruption due to shattering does not appear in this plot because it does not lead to grain mass loss to the gas other than through nonthermal sputtering during the slowing down of the fragments (§ 4.4), and the secondary effect on destruction due to the modified size spectrum (all of which are included in Fig. 13a). Figure 13b shows the graphite grain destruction and disruption as $dM/dt \times M^{-1} \times$ time, where M is the total initial grain mass per hydrogen nuclei, as a function of the shocked column of the gas. Equal areas under the curves correspond to equal fractions destroyed, or equal fractions disrupted in the case of shattering. Figures 13a and 13b show that the graphite grain destruction is dominated by nonthermal sputtering, and that about 80% of the grain destruction is due to this process in this shock. It is also clear from these figures that the peak destruction occurs at $N_H \sim 10^{17.5}$ cm^{-2}. In Figure 13b we have also plotted the shattering of the largest graphite grains ($a = 2100$ Å) in the size distribution. Note that the shattering dominates and that we have had to divide the shattering results by 200 in order to display them on the figure. The collisional destruction due to vaporization, and disruption due to shattering, peak a little later than nonthermal sputtering, i.e., at $N_H \sim 10^{17.6}$ cm^{-2}, because of the lower velocity thresholds for these processes. Figure 13c shows the masses in four graphite grain bins as a function of the shocked column of gas, and very dramatically shows the effects of grain shattering. Clearly, large grains ($a > 400$ Å) are rapidly disrupted in a single 100 km s^{-1} shock and the grain mass is transferred into smaller grains, the shattered fragments of the large grains. Also, note the very rapid rise, with increasing shocked column, in the mass transferred to the smallest grains.

Figures 14a, 14b, and 14c show the grain destruction and disruption as a function of the grain size for three shocks with $n_0 = 0.25$ cm^{-3}, $B_0 = 3$ μG, and velocities of 50 km s^{-1}, 100 km s^{-1}, and 200 km s^{-1}, respectively. In these plots the shattering data presented show the disruption and creation of grains of a given size, separately. Here we note the dramatic effects of shattering on the largest grains in our initial size distribution. Large grains ($a > 1000$ Å) are almost completely disrupted in all the shocks that we have studied. Note that the shattering loss term can fall below the vaporization loss; this occurs for grains that are rapidly decelerated by collisions with gas atoms, which are then destroyed by vaporization in collisions with fast-moving large grains. These figures also show the dominance of sputtering destruction over vaporization destruction. For $v_s \leq 150$ km s^{-1} nonthermal sputtering is dominant, but at $v_s = 200$ km s^{-1} the thermal sputtering destruction of the small grins is very clearly illustrated.

Results for 50, 100, 150, and 200 km s^{-1} shocks with $n_0 = 0.25$ cm^{-3} and $B_0 = 3$ μG are shown in Figures 15a, 15b, 16a, and 16b. In Figures 15a and 16a we show the percentage of grain mass destroyed as a function of the shock velocity for each destruction process, i.e., vaporization, nonthermal sputtering, and thermal sputtering. The effects of grain shattering are shown in Figures 15b and 16b, where the percentage of the grain mass affected by shattering is shown as a function of the shock velocity. In addition, in Figures 15b and 16b we show the percentage of the total
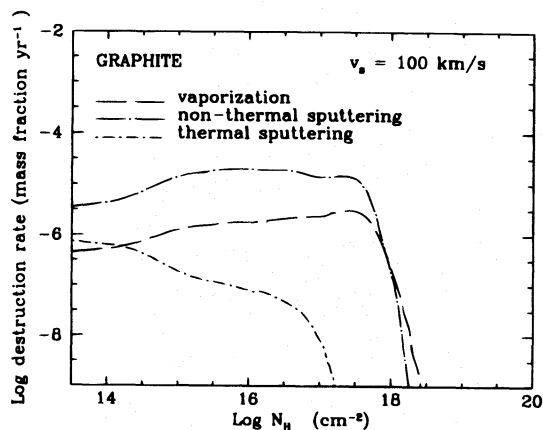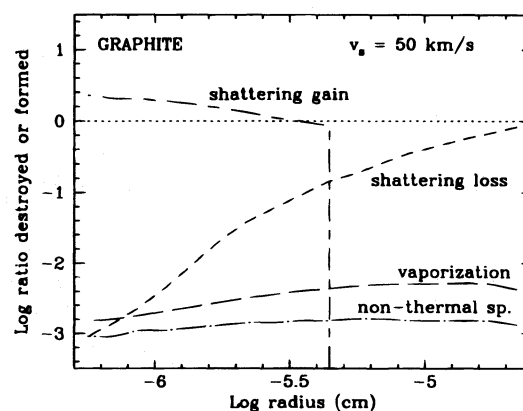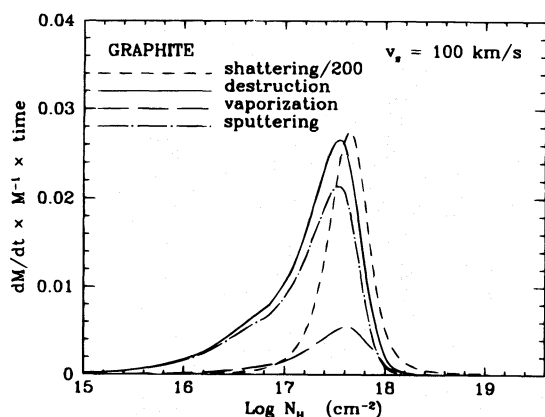

FIG. 12.—100 km s^{-1} "standard" shock profile (temperature, $T_4 = T_k/10^4$, density, n_H, and electron relative abundance, x_e) as a function of the shocked column density for $M_{A\perp} = 9.0$ (corresponding to $n_0 = 0.25$ cm^{-3} and $B_0 = 3$ μG). To convert column density ($N_H = n_0 v_s t$) to time: $\log t(\text{yr}) = \log N_H(\text{cm}^{-2}) - 13.9$. Also shown in the lower part of the plot are the graphite grain velocities as a function of shocked column density for three grain radii.

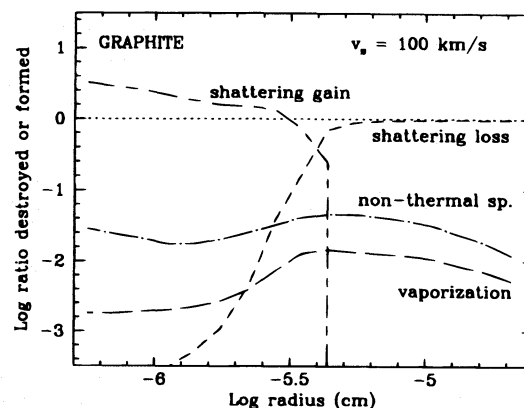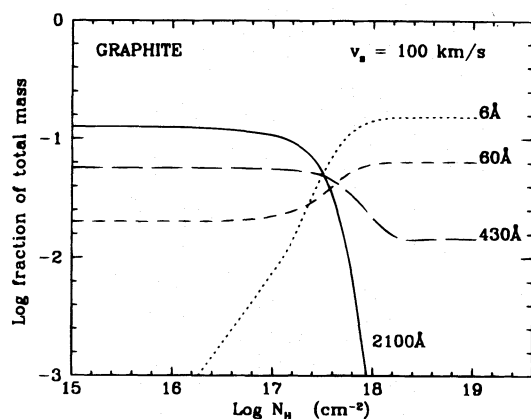FIG. 13a

FIG. 13b

FIG. 13c
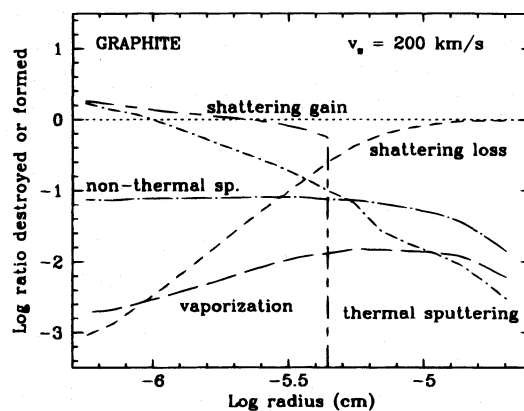

FIG. 14a

FIG. 14b

FIG. 14c

FIG. 13.—(a) Time-dependent graphite grain destruction rate (fraction destroyed per year) as a function of the shocked column density for vaporization and sputtering, for the "standard" shock of Fig. 12. (b) Total graphite destruction rate multiplied by time, and divided by total initial grain mass, plotted as a function of the shocked column density for collisional and sputtering destructive processes, for the "standard" 100 km s^{-1} shock. This plots grain fraction destroyed vs. shocked column, such that equal areas show equal destruction. Shattering so dominates that the shattering rate for the grains in the largest mass bin (radii = 2100 Å) is multiplied by 0.005 to fit on the figure. (c) Graphite grain bin masses for four grain radii plotted as a function of the shocked column density, for the "standard" 100 km s^{-1} shock. The 6 Å bin is empty at the start of the calculation. This plot clearly shows the rapid disruption of the largest grains, and the formation of small grains by shattering.

FIG. 14.—(a) Postshock graphite grain destruction, disruption, and formation as a function of radius, presented as ratio of initial to final bin mass, for shattering mass loss (short-dashed), shattering mass gain (short-dash–long-dashed), vaporization (long-dashed), nonthermal sputtering (nonthermal sp., dot-long-dashed), and thermal sputtering (dot-short-dashed) for $v_s = 50$ km s^{-1}. Also shown is the line for constant bin mass (dotted). (b) Same as for Fig. 14a, but for $v_s = 100$ km s^{-1}. (c) Same as for Fig. 14a, but for $v_s = 200$ km s^{-1}.

initial grain mass that ends up in grain fragments smaller than the smallest grain in our initial size distribution (<50 Å), and the percentage of the initial mass that ends up in the unprocessed dust bin (<14 Å) which includes all fragments with radii 5–14 Å.

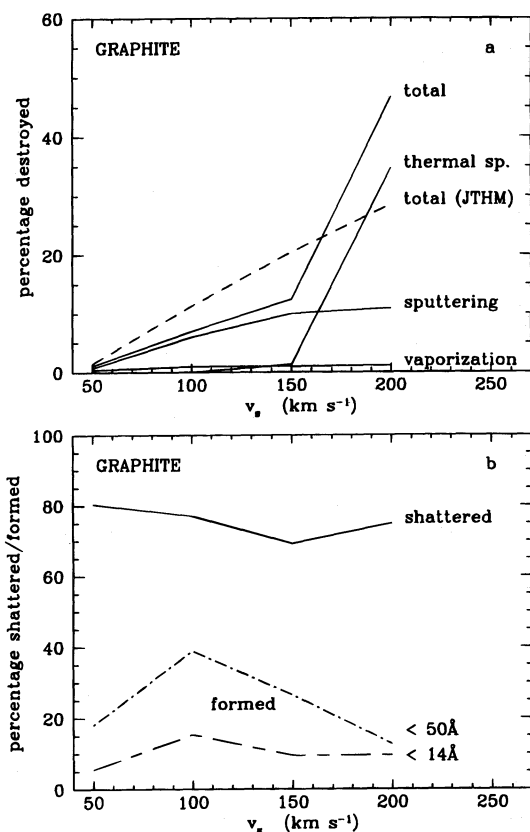From Figures 15a and 16a we conclude that nonthermal sputtering is the dominant grain destruction process for

FIG. 15.—(a) Postshock graphite grain destruction (mass percentage destroyed) as a function of shock velocity and destructive processes (thermal sp. refers to thermal sputtering, and sputtering refers to nonthermal sputtering) for fixed preshock density ($n_0 = 0.25$ cm^{-3}) and magnetic field ($B_0 = 3$ μG). Also shown, as total (JTHM), is the total destruction for shocks with no shattering in grain-grain collisions taken from Jones et al. (1994). (b) Postshock graphite grain shattering, i.e., percentage mass fraction of the total initial grain mass affected by shattering (shattered), and the fraction of the total initial grain mass that shattered into sub–50 Å fragments (<50 Å), and in sub–14 Å fragments (<14 Å) — (formed).

$v_s \leq 150$ km s^{-1}, which is in keeping with our previous results (Jones et al. 1994). However, we note that, for the 200 km s^{-1} shock, thermal sputtering dominates graphite grain destruction and is almost as important as nonthermal sputtering in the case of silicate grains. The dominance of thermal sputtering is due to the shattering of the large grains into smaller fragments; the associated increase in the total grain surface area leads to enhanced thermal sputtering in the hot postshock gas in high-velocity shocks (Tielens et al. 1994; Jones et al. 1994). The effects of vaporization in grain-grain collisions are reduced because shattering now dominates the grain-grain collisional processing. In previous calculations, with no shattering, the large grains, which show the greatest degree of collisional destruction, experience many collisions, each of which results in the vaporization of part of the grain before the grain is brought to rest with respect to the gas. However, with the inclusion of shattering, one grain-grain collision is typically sufficient to completely shatter a large grain into small fragments that stop quickly, and these fragments see few, if any, subsequent collisions with other grains (see § 4.3). Therefore, the overall level of grain vaporization is significantly reduced when shattering is taken into account.

Figure 17 shows the initial MRN and final grain size distributions, plotted as $n(a)$ versus radius, for single 50, 100,
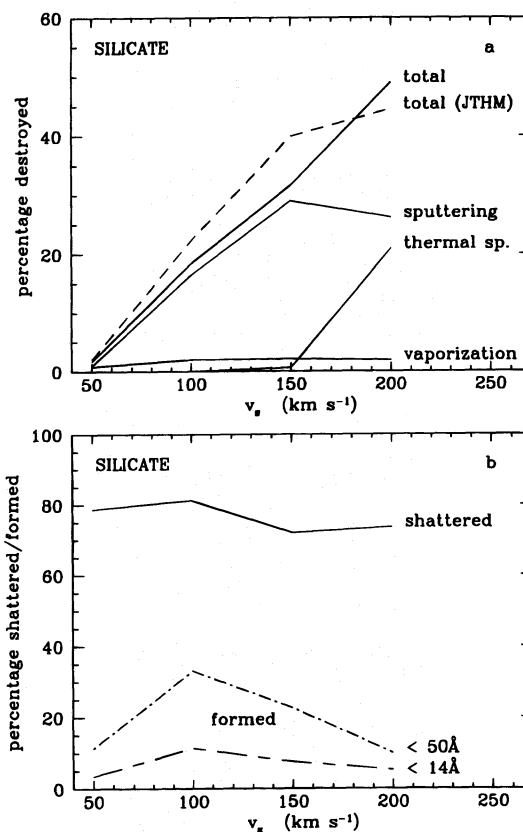
FIG. 16.—(a) Same as for Fig. 15a, but for silicate grains. (b) Same as for Fig. 15b, but for silicate grains.
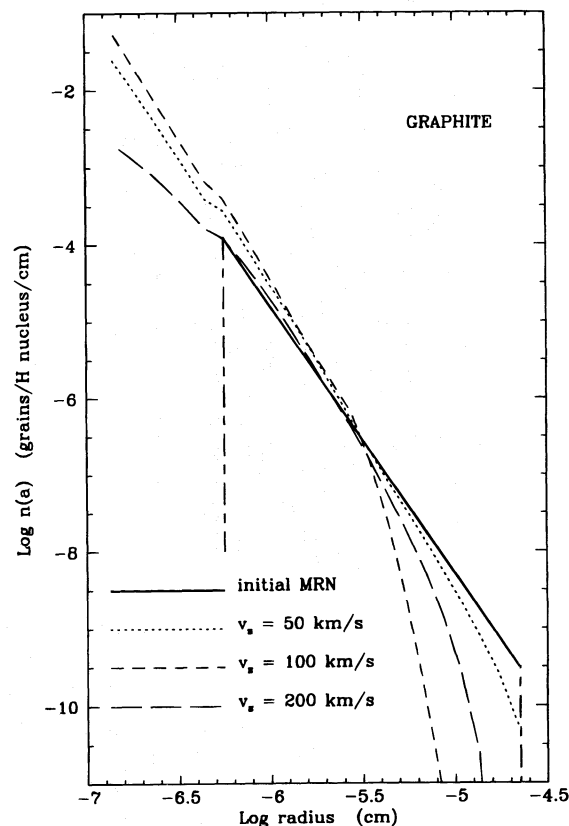
FIG. 17.—Graphite grain initial MRN (solid), and postshock size distributions for shock velocities of 50 km s^{-1} (dotted), 100 km s^{-1} (short-dashed) and 200 km s^{-1} (long-dashed).

and 200 km s^{-1} shocks. This clearly shows the loss of large grains with radii greater than 300 Å, and the formation of a significant number of small grains in a single shock. For the 200 km s^{-1} shock the large grain destruction and disruption is actually less than in the 100 km s^{-1} shock because in the faster shock the grains are not betatron accelerated. In Figure 17 note the change in slope of the size distribution for the 50 and 100 km s^{-1} shock cases, i.e., the final size distribution for the sub-300 Å grains is steeper than the initial MRN distribution despite the fact that the adopted shattered fragment size power-law index (-3.3) is less than that for the initial MRN size distribution index (-3.5). This is because the cumulative effects of fragmentation in grain-grain collisions in a grain size distribution, with differential velocities, lead to a steeper final grain size spectrum than the contributing fragmentation size spectrum (Biermann & Harwit 1980). The underlying reason for this is that the most energetic shattering events generate fragments whose upper size limit is very small (see eq. [29] for the upper limit fragment masses in the catastrophic collision regime). This effect can be seen in Figure 5, where the sum of fragment distributions for a range of collision velocities, for fixed projectile and target grains (e.g., 250 Å projectiles on 1000 Å targets), will yield a final size spectrum which is steeper than the shattered fragment size spectrum for an individual collision event.

In Figure 18 we show the effects of varying the power law of the shattered fragments, α_f, from 2.5 to 4.5, equivalent to $z = (\alpha - 1)/(4 - \alpha)$ ranging from 1 to -7. Clearly, changing the fragment power-law index has little effect on the final grain size distributions, even in the unphysical and extreme
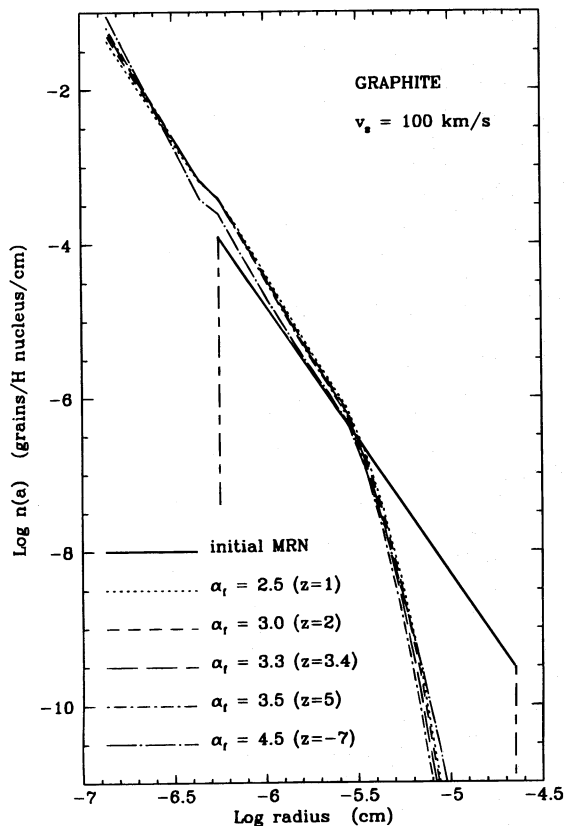
z cases ($z < 3$ or $z > 4$). In Figure 19 we show the effects of removing the velocity dependence of the maximum fragment radius in the catastrophic collision regime, i.e., we adopt $a_{f+} = 0.22a_T$ for catastrophic collisions in this case. Again, we find that the final size distribution is insensitive to this change in the fragment size distribution.

In Figure 20 we show the grain radius at which 50% of the grains survive, a_{half}, as a function of the shock velocity. Half of the grains with $a = a_{\mathrm{half}}$ survive the passage of a
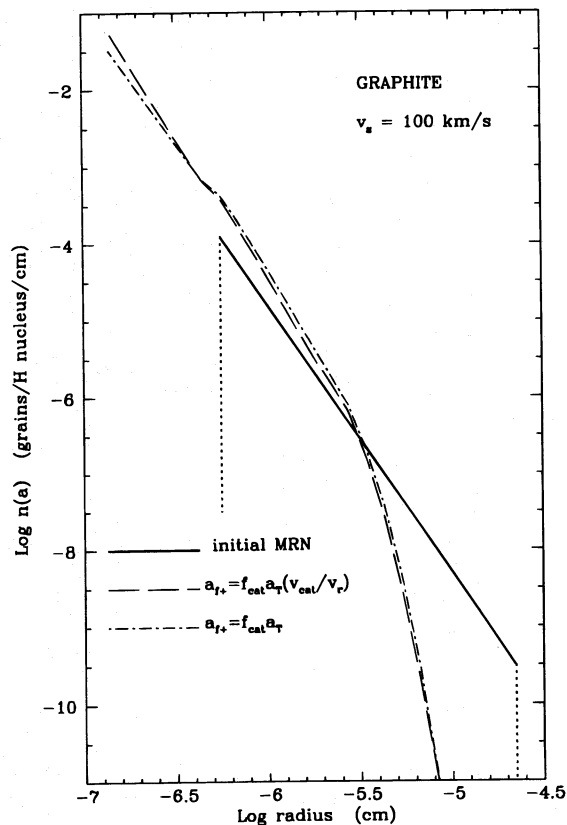

FIG. 19.—Graphite grain initial MRN (*solid*), and postshock size distributions for two catastrophic collision maximum shattered fragment expressions: the standard shock calculation with the velocity-dependent maximum fragment dimension (*dashed*), and for velocity independent maximum fragment sizes (*dash-dot*), for $v_s = 100$ km s^{-1}.
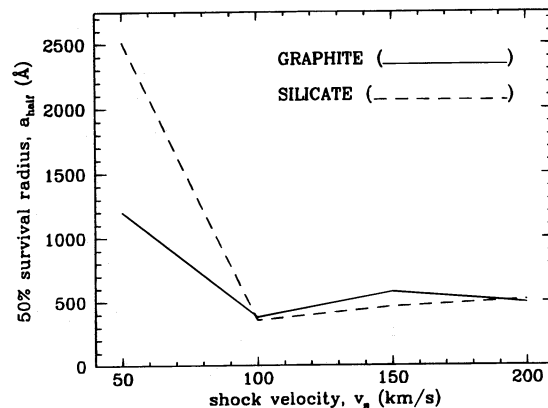

FIG. 18.—Graphite grain initial MRN (*solid*), and postshock size distributions for various shattered fragment power-law indices, α_f, ranging from 2.5 to 4.5 (equivalent to z values from 1 to -7) for $v_s = 100$ km s^{-1}.

FIG. 20.—Grain radius for which 50% of the initial grains survive the passage of a single shock, a_{half}, plotted against the shock velocity, v_s. Grains larger than a_{half} have a probability of less than a half of surviving the passage of a single shock.

single shock of velocity v_s, larger grains are disrupted. For grains with radii greater than a_{half} fewer than half of the original grains survive the passage of a single shock. Clearly, large grains survive better in the lowest velocity shock ($v_s = 50$ km s^{-1}). However, for $v_s \geq 100$ km s^{-1} $a_{half} \approx 500$ Å and is relatively insensitive to v_s. This is consistent with our findings that 1000 Å grains will see at least one catastrophic collision in shocks with velocities ≥ 100 km s^{-1}. In addition, we note that very large interstellar grains ($a \gg 1$ μm) will not undergo catastrophic collisions in shock waves because of the low abundance of grains with radii large enough to cause their catastrophic disruption. These very large grains will therefore be subject to sputtering only by atom or ion impacts and cratering due to small projectile impacts in shock waves. They will therefore survive passage through interstellar shocks with only minimal surface erosion.

The effects of shattering on the grain size distribution are clearly dramatic; for a wide range of initial grain size distributions the postshock size spectrum will likely look similar because of the disruption of the larger grains, and the prolific production of small fragments, with power-law size distributions, in grain-grain collisions. Therefore, the adoption of a different initial grain size spectrum would not greatly affect our conclusions regarding shattering. For example, the Kim et al. (1994) size distribution which has a minor fraction of very lage grains (0.5–3 μm) will yield very similar results. As emphasized above, the largest grains in this size distribution have only a low probability of experiencing a catastrophic collision, and hence, survive better than smaller ($\sim$3000 Å) grains. However, the largest fragments ($\sim$6000 Å) produced, if catastrophic collisions occur, will see so many further grain-grain collisions during slowing down (see Fig. 9) that they would quickly be ground down to sizes less than 300 Å (see § 4.3).

In Figure 21 we show the effects of preshock gas density on grain destruction, for fixed v_s and B_0. The percentage of the total grain mass destroyed is increased by factors of ≤ 2 for two orders of magnitude increase in the preshock density. The increased destruction arises from the increase in the betatron acceleration with increasing preshock density. This figure again shows the predominance of nonthermal sputtering in the destruction of grains in 100 km

s^{-1} shocks. Nonthermal sputtering accounts for $\approx$90% and $\approx$80% of the grain destruction for graphite and silicate, respectively. In Figure 21 we also show the total grain mass affected by shattering, which is very close to 80% for these shocks, i.e., all grains larger than 300 Å are disrupted by the shock.

Compared to our previous study (Jones et al. 1994) that did not include the effects of grain shattering, we find that the degree of grain destruction is reduced in all except the fastest shock considered ($v_s = 200$ km s^{-1}; Fig. 15a and 16a). The destruction, compared to the Jones et al. (1994) results, is reduced by a factor of $\approx$1.4–1.6 for graphite and by a factor of $\approx$1.2 for silicate, for $v_s \leq 150$ km s^{-1}. For $v_s = 200$ km s^{-1}, the grain destruction is increased by a factor of 1.6 for graphite and by a factor of 1.1 for silicate, compared to our previous results. For $v_s \leq 150$ km s^{-1} the shattering to small particles preserves the grains since the large grains now suffer fewer vaporizing collisions (see above). For $v_s = 200$ km s^{-1}, the shattering to small grains is followed by efficient (total) thermal sputtering of the tiny grains in the hot postshock gas.

In terms of the overall grain mass destruction (grain mass returned to the gas), shattering causes only modest changes in the results. The increase in thermal sputtering provides the most important difference with our earlier results. However, the most dramatic effect that we see when shattering is included in the grain shock processing scheme is the almost complete disruption of the largest grains in the size distribution and the production of large quantities of very small grains.

6. 1000 Å TEST PARTICLES

As in our previous study (Jones et al. 1994) we have undertaken a test particle study in which we follow individual particles through the shock profiles defined by the parameters in Table 2. The test particles are followed as they interact with size distributions of graphite and silicate "field particles," i.e., the initial MRN distributions and the subequent distributions that arise from the original grains as a result of shattering. These test particles are subject to thermal sputtering, nonthermal sputtering, vaporization and shattering, but they do not affect the destruction of the field particles, and they do not collide with, or interact with, each other. We consider spherical test particles of initial radius 1000 Å, and a range of particle materials, including graphite, silicate, silicon carbide, iron, diamond, and water ice.

In this paper we do not include any porous test particle calculations because it is not clear how the shattering of porous particles should be treated. Clearly, the shattering of porous grains is more complex because the disruption process for a porous grain, consisting of "coagulated" subgrains, will include the shattering of the subgrains as well as their disaggregation, i.e., the breaking of subgrain-subgrain contacts. Dominik & Tielens (1996) have studied the mechanics of porous particles and the physics of coagulation, but to date no model for the behavior of porous particles in grain-grain collisions in shock waves is available.

In Figure 22a we show the percentage destruction (by mass) of the test particles, for shock-velocities from 50 to 200 km s^{-1}. In these test particle calculations we follow the remnant grain after shattering collisions, but do not follow the evolution of the fragments arising from shattering
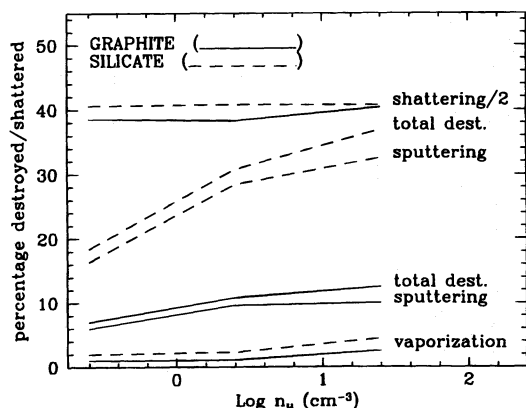

FIG. 21.—Postshock graphite (*solid*) and silicate (*dashed*) grain destruction and disruption as a function of preshock density, for fixed shock velocity ($v_s = 100$ km s^{-1}) and magnetic field ($B_0 = 3$ μG); for the destructive process of vaporization, and sputtering (nonthermal and thermal), and for the disruptive process of shattering (divided by 2).
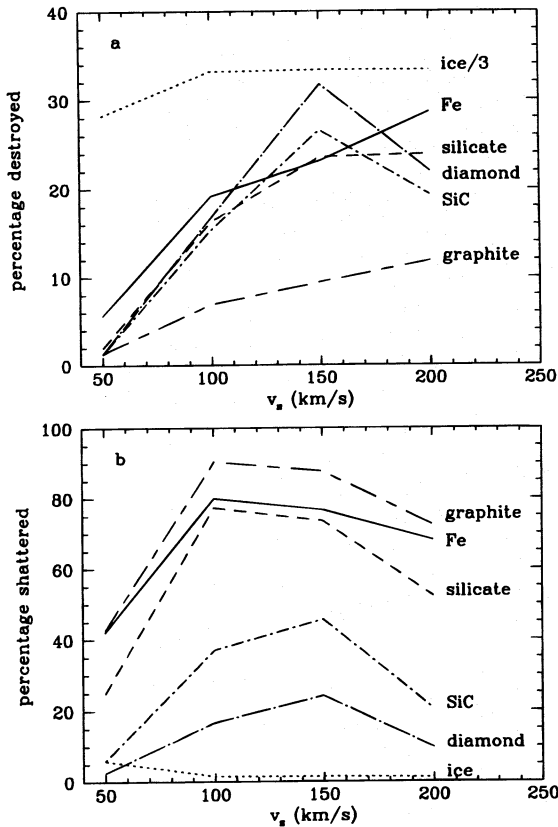
FIG. 22.—(a) Test particle ($a = 1000$ Å) percentage destruction (by mass) as a function of shock velocity for six grain materials. The ice data have been multiplied by a factor of 0.33. (b) Test particle ($a = 1000$ Å) percentage shattering disruption (by mass) as a function of shock velocity for the same materials as in Fig. 19.

events on that particle, i.e., all mass loss from the test particle, whether through sputtering, vaporization, or shattering, is considered to be erosion of the original 1000 Å test particle. Compared to our previous results, which do not include the effects of shattering, we find that the total mass loss from the 1000 Å test particles, due to destruction and disruption, is enhanced by factors of about 2–5, due primarily to shattering in grain-grain collisions. In a 100 km s^{-1} shock, ice particles are almost completely destroyed by sputtering regardless of whether or not shattering is included. Figure 22b shows the percentage disruption by shattering, and it is clear that, with the exception of ice, shattering is a major, and in most cases the dominant, 1000 Å grain loss process, i.e., the grains are shattered into smaller fragments which evolve differently from the parent grains. For ice, shattering is unimportant and sputtering dominates because of the low thresholds for this material (Tielens et al. 1994; see Table 1 for a comparison of the sputtering parameters of ice with the other more refractory materials). Thus ice particles are easily destroyed in low-velocity shocks. We also note significant destruction of the graphite, silicate, and iron particles at shock velocities ≥ 100 km s^{-1}. The large degree of iron particle destruction and disruption, despite it being more resistant to shattering, is due to its high specific mass density and the resultant betatron acceleration to large postshock velocities (15%–35% higher than for silicate grains). We also note the resistance of diamond and silicon carbide grains to shattering; however, they still do undergo significant sputtering in these calculations (for diamond we

use the same sputtering parameters as for graphite; see Tielens et al. 1994).

7. GRAIN LIFETIMES

Following McKee (1989) we have calculated the time-scale for supernova shock waves to destroy interstellar dust (i.e., to return the grain mass to the gas) in all phases of the interstellar medium, t_{SNR}, and the equilibrium fraction of the elements locked up in refractory grains in the interstellar medium, δ_{eq}. For the sake of clarity we reproduce the required formulae here; i.e.,

$$t_{SNR} = \frac{9.7 \times 10^7}{\int \epsilon(v_{s7})/v_{s7}^3 \, dv_{s7}} \text{ yr}, \qquad (40)$$

and

$$\delta_{eq} = \delta_{in} \left[1 + \frac{t_{in}}{t_{SNR}} \right]^{-1}, \qquad (41)$$

where v_{s7} is the shock velocity (in units of 100 km s^{-1}); $\epsilon(v_{s7})$ is the efficiency of grain destruction for a shock of velocity v_{s7}; δ_{in} is the dust fraction in the material injected into the interstellar medium from stellar sources (we assume a value of 0.9 for graphite and silicate, a rather generous estimate); and t_{in} is the timescale for the injection of refractory elements into the interstellar medium by mass loss from evolved stars and matter synthesized in supernovae (we assume a value of $t_{in} = 2.5 \times 10^9$ yr from Jones & Tielens 1994).

From the calculated grain destruction data (§ 5 and Table 4) we have derived analytical expressions for $\epsilon(v_{s7})$ for the graphite and silicate MRN grain populations and present the fitted parameters in Table 5A. These analytical fits are a good approximation to the data in Table 4 for 50 km s$^{-1} \leq v_s \leq 200$ km s^{-1}. In these calculations we use linear extrapolations of these data to zero grain destruction

TABLE 5

A. GRAIN DESTRUCTION ANALYTICAL FIT PARAMETERS

Grain	Velocity Range (km s^{-1})	c	d
Graphite (MRN)......	41–100	0.12	0.05
	100–150	0.11	0.04
	150–300	0.69	0.91
Silicate (MRN)........	45–100	0.33	0.15
	100–150	0.26	0.08
	150–300	0.35	0.21

$$\epsilon(v_{s7}) = cv_{s7} - d$$

B. LARGE GRAIN DESTRUCTION AND DISRUPTION ANALYTICAL FIT PARAMETERS

Grain	Velocity Range (km s^{-1})	g	h
Graphite ($a \geq 1000$ Å)......	40–50	6.52	2.61
	50–100	0.70	−0.30
	100–150	0.00	−1.00
	150–300	−0.03	−1.05
Silicate ($a \geq 1000$ Å)........	40–50	3.78	1.51
	50–100	1.23	0.24
	100–150	0.02	−0.97
	150–300	−0.09	−1.13

$$\epsilon(v_{s7}) = gv_{s7} - h$$

(equivalent to shocks of velocity 41 km s^{-1} and 45 km s^{-1}, respectively, for graphite and silicate grains), and to 300 km s^{-1} shocks. We find grain lifetimes for the MRN distributions of $t_{SNR} = 6.3 \times 10^8$ yr and 3.7×10^8 yr for graphite and silicate grains, respectively; N.B., these are the time scales to return the entire grain mass to the gas as atoms. For the equilibrium fractions of the elements locked into dust in the interstellar medium we find $\delta_{eq} = 0.18$ and 0.12, for graphite and silicate, respectively. The inclusion of shattering in the shock code increases the derived grain lifetimes by factors of ≈ 1.1 for both graphite and silicate, and the δ_{eq} values increase by similar amounts.[8] The comparisons here are with our previous results (increased by a factor of 1.5) that do not include shattering (Jones et al. 1994). However, the increased lifetimes still fall short of the dust lifetimes of $t_{SNR} \geq 2 \times 10^{10}$ yr (Jones et al. 1994) required to preserve $\geq 90\%$ of the stellar ejected silicates in the interstellar medium (Draine & Lee 1984; Mathis 1990). Therefore, we still cannot solve the well-known conundrum (see Barlow 1978a , 1978b; Draine & Salpeter 1979a, 1979b; Dwek & Scalo 1980; Seab & Shull 1983; McKee et al. 1987; Jones et al. 1994): Why is silicate dust so abundant (possibly containing 90% of elemental silicon) in the interstellar medium? Moreover, this marginally increased lifetime is gained at the expense of the complete disruption of the largest grains in the size distribution; the large grains being shattered into more resilient smaller particles. Shattering therefore adds a new conundrum: Why do visual extinction measurements show that most of the mass in interstellar dust is in large grains (radii ≥ 0.1 μm)?

Given that the inclusion of grain shattering in grain-grain collisions into the grain processing scheme leads to the almost complete elimination of large grains ($a \geq 1000$ Å) from the grain populations in a single fast (100 km s^{-1}) shock, we calculate the disruption and destruction time scales (disruption dominates), t_{dd}, for these large interstellar grains in interstellar shock waves. N.B., this is the time scale to disrupt all large grains in the interstellar medium and to shatter them into sub-500 Å fragments in grain-grain collisions in shock waves. We use the same method as for calculating the MRN grain population lifetimes, equating t_{dd} with t_{SNR} from equation (43), and present the analytical fit data in Table 5B. The grain disruption parameters here have been calculated by comparing the preshock and postshock masses in the first four mass bins in our numerical scheme, equivalent to grains of radii ≥ 1000 Å. In the initial MRN size distributions over 40% of the grain mass is in grains with radii 1000–2500 Å. Also, we assume that there is no grain disruption in shocks with velocities less than 40 km s^{-1}, in order to provide a direct comparison with the MRN grain lifetime calculations above. If, as seems likely given the low-velocity thresholds (~ 1 km s^{-1}), shattering is important in shocks with $v_s \leq 40$ km s^{-1}, then our disruption time scales will be upper limits. The derived large-grain disruption time scales are $t_{dd} \leq 5.1 \times 10^7$ yr and $\leq 6.5 \times 10^7$ yr for graphite and silicate, respectively, and are factors 12 (graphite) and 6 (silicate) times smaller than the destruction lifetimes, t_{SNR}, calculated above. The equivalent equilibrium fractions of the elements locked into grains larger than 1000 Å are ≤ 0.02 for both graphite and silicate.

We conclude from this that large graphite and large silicate grains have short disruption time scales in the diffuse interstellar medium. This implies that any large interstellar grains must be formed in the interstellar medium; i.e., by accretion/condensation to form large homogeneous grains and/or through coagulation to form large porous/fractal grains. The monomers and/or cores likely have radii less than about 500 Å.

Our test particle calculations confirm the large-grain disruption time scales, for example, for 1000 Å graphite, silicate, and iron grains we find $t_{dd} \sim 6$–8×10^7 yr. However, for the tougher silicon carbide and diamond grains of radius 1000 Å we find $t_{dd} \sim 2 \times 10^8$ yr, or about a factor of 3 longer than for graphite, silicate, and iron.

For our ice test particle lifetime calculations, i.e., lifetime against sputtering destruction in the interstellar medium, we assume no destruction in shocks with velocities less than 1 km s^{-1}, and find that ice can survive in the diffuse interstellar medium for $\sim 10^6$ yr. This is of the same order as the time interval between shocks of a few tens of kilometers per second. Thus we confirm that ice grains are easily destroyed in low-velocity shocks.

8. PAH AND SMALL GRAIN FORMATION IN SHOCKS

From the results that we present in § 5 it is clear that grain shattering plays an important role in the redistribution of grain mass, i.e., small grains are readily formed from large grains in shocks in the interstellar medium. Figures 13c, 15b, 16b and 17 clearly show this mass transfer. Indeed, as much as 40% of the starting graphite grain mass may end up in sub–50 Å fragments, and 5%–15% of the starting graphite grain mass can end up in sub–14 Å fragments in a single fast shock. These latter fragments (< 14 Å) are of the same dimensions as the interstellar PAH (polycyclic aromatic hydrocarbon) molecules, or PAH clusters, that are inferred to be present in many interstellar and circumstellar environments (see Tielens 1990).

From our shock calculations we find that $\sim 5\%$ of the initial graphite grain mass, or $\sim 3\%$ of the cosmic carbon, ends up in 5–14 Å radius fragments for single shocks with $v_s \equiv 50$ km s^{-1}. The maximum graphite grain mass converted into small grains appears to be about a factor of 3 higher than the above values and occurs in the 100 km s^{-1} shock. Thus, one 100 km s^{-1} shock, or several 50 km s^{-1} shocks, would be sufficient to put enough of the graphite grain mass into small graphite grains in order to explain the required fraction of interstellar carbon in PAHs and PAH clusters ($\sim$ few percent; Tielens 1990).

One prediction of this model is that, besides the PAH population, there should be a similar population of small silicates in the interstellr medium. However, there is a structural difference between small silicate and graphite grains which likely affects the shattering outcome. Graphite grains have a layered structure with a binding energy between the layers of $\sim 7 \times 10^{-4} N_C$ eV, with N_C the number of carbon atoms in a layer compared to C—C bond energies of 5.7 eV. Hence, shattered graphitic fragments with sizes less than 30 Å ($\leq 10^3$ carbon atoms) will have binding energies between their individual layers of less than 1 eV. Likely, such fragments will actually shatter into sheetlike structures with typically a few hundred carbon atoms. Alternatively, such a loosely bound small conglomerate may actually fall apart upon far-ultraviolet photon absorption (Tielens 1993). In contrast, interstellar silicates are thought to have three-

---

[8] We have reevaluated our previous results, using the same type of analytical fit to the data that we adopt in this paper, and find that our previous results for t_{SNR} and δ_{eq} should be increased by a factor of 1.5.

dimensional structures. Thus, while silicate grains may be shattered into small spherical fragments with sizes in the range 10–30 Å or so, the graphitic grains are expected to be ground down into two-dimensional PAH molecules or PAH clusters.

Observationally, the presence, or absence, of small silicate grains in the diffuse interstellar medium is not well established, although Désert et al. (1986) have put an upper limit of 1% on the fraction of the silicate mass that can be in very small grains (the launch of the *Infrared Space Observatory* will likely lead to observations that reveal the nature of the small interstellar grains in detail). However, interstellar dust exposed to strong far-ultraviolet radiation (i.e., near H II regions or in reflection nebulae) shows a mid-infrared emission spectrum dominated by molecular-sized PAHs (~ 50 carbon atoms) and PAH clusters (~ 500 carbon atoms). The tell-tale signature of small silicates—the 10 μm emission feature—is notably absent. Whether this reflects on the smallest silicate fragments produced by shattering or the unimportance of shattering, in general, in these environments, remains to be seen.

9. CONCLUSIONS

We have undertaken an extensive study of the effects of shattering in grain-grain collisions. Based upon extensive numerical simulation of surface explosions and impacts, we have developed an analytical model which calculates the final crater mass, and fragment size distribution, in grain-grain collisions as a function of the collision velocity, grain sizes, and grain material properties. The model contains one free parameter, the critical shock pressure for shattering, and we find good agreement with laboratory experiments, on (sub)micron-sized impacts on a wide variety of materials, assuming that the critical pressure for shattering is equal to the shear strength of the material. The threshold grain-grain collision velocities are of order 1 km s^{-1} for shattering. The shattering threshold pressure is about an order of magnitude smaller than that for vaporization, and we conclude that the effects of shattering will dominate over vaporization in grain-grain collisions. The shattered fragment size distribution scales with the $a^{-3.3}$, slightly less steep than the MRN size distribution. In general, any shattering model where the fragment size distribution is related to the shock pressure will lead to power-law size distributions of the fragments with indices slightly steeper than ~ 3. We find that the maximum fragment size increases with increasing collision velocity, until the target grain is completely disrupted by the collision, and for higher velocity collisions we predict that the maximum grain size then decreases with velocity.

Grains are destroyed (returned to the gas) in interstellar shock waves mainly through sputtering. In high-velocity shocks ($v_s > 150$ km s^{-1}) graphite grains are predominantly destroyed by thermal sputtering, while silicate grains are almost equally destroyed by nonthermal and thermal sputtering. In lower velocity shocks ($v_s \leq 150$ km s^{-1}), grain destruction is principally though nonthermal sputtering driven by the betatron acceleration of the grains. The vaporization of grains in grain-grain collisions is found to be an unimportant grain destruction process. Our treatment of the processing of grains in shocks now includes the shattering of grains in grain-grain collisions, and the inclusions of this process leads to the disruption of large grains (radii > 1000 Å) into smaller fragments (radii < 500 Å, for

an initial MRN distribution), and has dramatic effects upon the evolution of the size distribution of the grains through the shock.

Large grains ($a > 1000$ Å) are readily disrupted in interstellar shock waves by shattering in grain-grain collisions. The disruption of these large grains is almost complete for single shocks with velocities $v_s \geq 100$ km s^{-1}, implying that the disruption time scales for large grains in the interstellar medium, t_{dd}, are of order 50–60 million yr. However, the inclusion of shattering into the grain *destruction* scheme actually leads, overall, to lower levels of grain destruction and longer grain lifetimes, t_{SNR} of 6×10^8 yr and 4×10^8 yr for MRN size distributions of graphite and silicate grains, respectively, compared to calculations that neglect grain shattering (Jones et al. 1994).

The increase in the lifetime of grains with MRN size distributions, when shattering is included in the grain-grain collision processing, is due to the second-order effects of shattering. With vaporizing-only collisions, which predominantly affect the largest grains (radii ≥ 1000 Å) which attain the highest postshock velocities, a grain in a shock wave experiences many collisions with small particles before it is brought to rest with respect to the gas. These collisions erode the large grains and transfer grain mass to the gas. With the inclusion of shattering, one collision of a small grain with a larger grain is sufficient to fragment a significant fraction of that larger grain, because of the lower thresholds for shattering than for vaporization. One grain-grain collision will therefore fragment a large grain into smaller fragments which are rapidly slowed by collisions with gas atoms. At rest the only collisions that the fragments experience are with the small abundance of remaining large grains that are still in motion with respect to the gas. Therefore, shattering reduces the effects of vaporization destruction by redistributing the grain mass into smaller, more resilient fragments.

Grain shattering in grain-grain collisions leads to major changes in the grain size distribution; in particular, large grains are ground down into smaller grains and the resulting size distribution is somewhat steeper, and shifted to smaller grains, than an initial MRN distribution. This result is relatively insensitive to the fragment size distribution (in our model, the fragment size distribution is shallower than the MRN distribution). It appears likely that shock fragmentation of graphite grains can be a major source of PAH molecules, PAH clusters, and small carbon grains in the interstellar medium. There should also be a population of small silicate grains. However, in view of the difference in solid structure we do not expect a silicate analog to the (molecular) PAH population.

In this study we are therefore not able to answer the question: Why is dust, and in particular silicate dust, so abundant in the interstellar medium? All work on this subject shows that dust is readily destroyed in interstellar shock waves. Thus, we conclude that grain growth must occur in some phase of the interstellar medium, in order to explain the observed depletions of the refractory elements into interstellar dust. Our previous paper (Jones et al. 1994) proposed some possible scenarios that are consistent with the observational constraints and with the dust destruction model presented in that paper.

However, we now add to the problem because the work presented in this paper shows that large grains are rapidly disrupted in shock waves. Thus, the reformation of large

grains in the interstellar medium must be efficient in order to account for the large fraction (by mass) of grains with radii ≥ 1000 Å. These large interstellar grains are most likely reformed by coagulation and accretion in dense clouds. Accretion alone cannot reform the very largest grains because only relatively thin mantles can accrete; thus coagulation is the most likely large grain reformation mechanism. However, coagulation is only important in dense regions with $n_H \gg 10^3$ cm^{-3} (Chokshi, Tielens, & Hollenbach 1993). Coagulation implies that the large interstellar grains may be rather porous. In particular, we conclude that interstellar grains with radii 500 Å to ≈ 1 μm should be porous, while very large grains with radii larger than a few microns may remain homogeneous because they do not undergo catastrophic collisions in interstellar shock waves. Our previous work on porous grains (Jones et al. 1994) indicates that porous grains may survive better than

solid homogeneous particles in shock waves because they are not betatron-accelerated. However, a full analysis of this problem will await a rigorous model for the properties of three-dimensional porous grains in collision with smaller solid particles and with other porous grains.

APPENDIX A

SHOCK WAVE PROPAGATION IN SOLIDS

Consider a normal incident impact of a projectile with mass, M_P, and velocity, v_r, on a slab. The shock velocity, v_s, and velocity of the shocked material, v_1, (in the frame of the unshocked material) for solids is often well represented by

$$v_s = c_0 + s v_1 , \tag{A1}$$

where c_0 is and s are material constants (Table 2). The Mach number, $\mathscr{M}_1$, corresponding to a critical pressure, P_1, is then given by

$$\mathscr{M}_1 = \frac{2\phi_1}{1 + (1 + 4s\phi_1)^{1/2}} , \tag{A2}$$

where

$$\phi_1 \equiv \frac{P_1}{\rho_0 c_0^2} . \tag{A3}$$

The target mass, M, shocked to the critical pressure is then given by

$$\frac{M}{M_P} = \frac{(1 + 2\mathscr{R})}{(1 + \mathscr{R})^{16/9}} \frac{1}{\sigma_{1i}^{1/9}} \left(\frac{M_r^2}{\sigma_1 \mathscr{M}_1^2} \right)^{8/9} , \tag{A4}$$

where $\mathscr{R}$ is given by

$$\mathscr{R} \equiv \left(\frac{s\rho_0}{s_P \rho_P} \right)^{1/2} , \tag{A5}$$

and σ is a weak function of the shock parameters; viz.,

$$\sigma \simeq \frac{0.30(s + \mathscr{M}^{-1} - 0.11)^{1.3}}{s + \mathscr{M}^{-1} - 1} \tag{A6}$$

evaluation at $\mathscr{M}_1$ for σ_1 and $\mathscr{M}_r/(1 + \mathscr{R})$ for σ_{1i}.

APPENDIX B

THE COMPUTATIONAL SCHEME FOR GRAIN SHATTERING

Following Jones et al. (1994) we have cast our equations in terms of mass bins in order to ensure mass conservation, and we refer the reader to our earlier work for the details of this procedure.

Numerically, shattering is treated in the same manner as vaporization in the method of Jones et al. (1994), with a modification for the placement of the shattered fragments into the appropriate mass bins. This is in contrast to our previous work where a single remnant particle is produced by vaporization of two grains in a given grain-grain collision. The modification to the code involves the inclusion of a further pair of terms for shattering, one a loss term and the other a gain term, analogous to those for vaporization (for comparison, see the first and third terms in eq. [A6] in Appendix A of Jones et al. 1994). For the shattering of a single grain component we therefore have for the rate of change of the mass in the kth bin

(M_k);

$$\frac{dM_k(\text{shattering})}{dt} = -\bar{m}_k \rho_k \delta_k \sum_{i=1}^{k_{\max}} \alpha_{ik} \rho_i \delta_i + \sum_{i=1}^{k} \sum_{j=1}^{k_{\max}} \alpha_{ij} \rho_i \delta_i \rho_j \delta_j m_{\text{sh}}(k) , \tag{B1}$$

$$\alpha_{ik} = \frac{\sigma(m_i, m_k) v(m_i, m_k)}{m_i m_k} , \tag{B2}$$

where $\rho_k = \bar{m}_k n(\bar{m}_k)$ is the kth bin particle mass density per unit mass interval, $\bar{m}_k$ is the mean bin mass, and δ_k is the bin width, $k_{\max}$ is the number of mass bins in the computation, $\sigma(m_i, m_k)$ is the grain-grain collision cross section, and $v(m_i, m_k)$ is the relative collision velocity. $m_{\text{sh}}(k)$ is the total mass of the shattered fragments of the ith particle in the collision of ith and jth particles that lies within the mass bounds of the kth bin.

In a given collision a fraction of the target grain mass, f_{vap}, is vaporized and some fraction, f_{sh}, of the remaining grain fragment is shattered. The fractions f_{vap} and f_{sh} are calculated independently, but shattering is assumed to be subordinate to vaporization. Therefore, f_{sh} is taken to be the minimum of f_{sh} or $(1 - f_{\text{vap}})$, i.e., $(f_{\text{vap}} + f_{\text{sh}})$ is always ≤ 1, and so the remaining mass (remnant) of the target after collision with another grain is $(1 - f_{\text{vap}} - f_{\text{sh}}) m_{\text{target}}$, and the total mass of the shattered fragments, $m_{\text{sh}} = f_{\text{sh}} m_{\text{target}}$, is assumed to have a power-law mass distribution with index γ, i.e.,

$$dn(m_f) = F_i m_f^{-\gamma} dm_f \tag{B3}$$

$$m_{f-} \leq m_f \leq m_{f+} , \tag{B4}$$

where m_{f-} and m_{f+} are the minimum and maximum shattered fragment masses, respectively. Thus,

$$f_{\text{sh}} m_{\text{target}} = \int_{m_{f-}}^{m_{f+}} \frac{dn(m_f)}{dm_f} m_f dm_f = F_i \int_{m_{f-}}^{m_{f+}} m_f^{1-\gamma} dm_f . \tag{B5}$$

The parameter F_i is determined by the total shattered mass, but is never determined because the shattered mass in a given bin is calculated as a fraction of the total shattered mass, i.e.,

$$m_{\text{sh}} = F_i \int_{m_{f-}}^{m_{f+}} m_f^{1-\gamma} dm_f = \frac{F_i}{(2-\gamma)} (m_{f+}^{2-\gamma} - m_{f-}^{2-\gamma}) , \tag{B6}$$

and the shattered mass in the kth bin,

$$m_{\text{sh}}(k) = F_i \int_{\eta_k m_{k+}}^{m_{k+}} m_f^{1-\gamma} dm_f = \frac{F_i}{(2-\gamma)} \left[m_{k+}^{2-\gamma} - (\eta_k m_{k+})^{2-\gamma} \right] , \tag{B7}$$

where η_k is the mass binning interval. Hence, for the case where all the mass bins are of the same interval, the fraction of the total shattered mass in the kth bin is

$$\frac{m_{\text{sh}}(k)}{m_{\text{sh}}} = \frac{(1 - \eta_k^{2-\gamma}) m_{k+}^{2-\gamma}}{m_{f+}^{2-\gamma} - (\eta_k m_{f-})^{2-\gamma}} . \tag{B8}$$

The minimum and maximum shattered fragment masses, m_{f-} and m_{f+}, used in the calculations are described in § 2 (where the equivalent minimum and maximum fragment sizes, a_- and a_+, are derived) and are based upon fits to laboratory data for the impact of submicron spherical projectiles upon planar targets. Otherwise the numerical method adopted is exactly the same as that of Jones et al. (1994), and we refer the reader to that work for a full description of the scheme we use in the calculations presented here.

In our calculations the actual shattered mass that is returned to the mass bins may be less than the total shattered mass because we have taken into account the sputtering destruction of fragments during their slowing down with respect to the gas (see § 4.4). The mass loss through sputtering depends solely upon the initial injection velocity of the fragments (with respect to the gas), and so is easily incorporated into the code because it is independent of the fragment mass. Thus, the actual shattered mass returned to the mass bins is $(1 - \phi) m_{\text{sh}}$, where ϕ is the fraction of the total fragment mass lost through sputtering during slowing.

REFERENCES

Allen, C. W. 1983, Astrophysical Quantities (London: Athlone)
Austin, M. G., Thomsen, J. M., & Ruhl, S. F. 1981, Proc. Lunar Planet. Sci. Conf., 12th, 1689
Austin, M. G., Thomsen, J. M., Ruhl, S. F., Orphal, D. L., Borden, W. F., Larson, S. A., & Schultz, P. H. 1981b, in Multi-Ring Basins, ed. P. H. Schultz & R. B. Merrill (Houston: Lunar Planetary Institute), 197
Barlow, M. J. 1978a, MNRAS, 183, 367
———. 1978b, MNRAS, 183, 397
Biermann, P., & Harwit, M. 1980, ApJ, 241, L105
Bjork, R. L., Kreyenhagen, K. N., & Wagner, M. H. 1967, Analytical Study of Impact Effects as Applied to the Meteoroid Hazard, NASA CR-757
Bland, D. R. 1964, Inst. Math. Appl., 1, 56
Borkowski, K. J., & Dwek, E. 1995, ApJ, 454, 254

Bushman, A. V., Kanel, G. I., Ni, A. L., & Forlov, V. E. 1993, in Intense Dynamic Loading of Condensed Matter (London: Taylor & Francis), p. 147
Chokshi, A., Tielens, A. G. G. M., & Hollenbach, D. 1993, ApJ, 407, 806
Cowie, L. L. 1978, ApJ, 225, 887
Croft, S. K. 1980, Proc. Lunar Planet. Sci. Conf., 11th, 2347
Désert, F. X., Boulanger, F., Léger, A., Puget, J. L., & Sellgren, K. 1986, A&A, 159, 328
Dienes, J. K., & Walsh, J. M. 1970, in High-Velocity Impact Phenomena, ed. R. Kinslow (New York: Academic), 46
Dohnanyi, J. S. 1978, in Cosmic Dust, ed. J. A. M. McDonnell (New York: Wiley), 527
Dominik, C., & Tielens, A. G. G. M. 1996, in preparation

Draine, B. T., & Lee, H. K. 1984, ApJ, 285, 89
Draine, B. T., & Salpeter, E. E. 1979a, ApJ, 231, 77
———. 1979b, ApJ, 231, 438
Dwek, E., & Scalo, J. M. 1980, ApJ, 239, 193
Fechtig, H., Nagel, K., & Pail, N. 1980, in Solid Particles in the Solar System, ed. I. Halliday & B. A. McIntosh (Dordrecht: Reidel), 357
Fechtig, H., Nagel, K., Stahle, V., Grögler, N., Schneider, E., & Neukum, G. 1977, Proc. Lunar Planet. Sci. Conf., 7th, 889
Fujiwara, A., & Tsukamoto, A. 1980, Icarus, 44, 142
Grady, D. E. 1981, Appl. Phys. Lett., 38, 825
Horie, Y. 1980, Phys. Rev. B21, 5549
Jones, A. P., & Tielens, A. G. G. M. 1994, in The Cold Universe, 13th Moriond Astrophysics Meeting, ed. T. Montmerle, C. J. Lada, I. F. Mirabel, & J. Tran Thanh Van (Gif-sur Yvette: Edi. Frontières), 35
Jones, A. P., Tielens, A. G. G. M., Hollenbach, D. J., & McKee, C. F. 1994, ApJ, 433, 797
Kim, S. H., Martin, P. G., & Hendry, P. D. 1994, ApJ, 422, 164
Kittel, P. 1976, Introduction to Solid State Physics (New York: Wiley)
Kreyenhagen, K. H., & Schuster, S. H. 1977, in Impact and Explosion Cratering, ed. D. J. Roddy, R. O. Pepin, & R. B. Merrill (New York: Pergamon), 983
Liffman, K., & Clayton, D. D. 1989, ApJ, 340, 853
Mandeville, J. C. 1972, Earth Planet. Sci. Lett., 15, 110
Mandeville, J. C., & Vedder, J. F. 1971, Earth Planet. Sci. Lett., 11, 297
Marsh, S. P. 1980, LASL Shock Hugoniot Data (Berkeley: Univ. California Press)
Mathis, J. S. 1990, ARA&A, 28, 37
Mathis, J. S., Rumpl, W., & Nordsieck, K. H. 1977, ApJ, 217, 105 (MRN)
Maxwell, D. E. 1973, Cratering Flow and Crater Prediction Methods, TCAM 73-17 (San Leandro: Physics Internat. Co.)
———. 1977, in Impact and Explosion Cratering, ed. D. J. Roddy, R. O. Pepin, & R. B. Merrill (New York: Pergamon), 1003
Maxwell, D. E., & Seifert, K. 1976, Modeling of Cratering, Close-In Displacements, and Ejecta, DNA-001-74-C-0151 (San Leandro: Physics Internat. Co.)

McDonnell, J. A. M., Flavill, R. P., & Carey, W. C. 1976, Proc Lunar. Planet. Sci. Conf. 7th, 1055
McKee, C. F. 1989, in Interstellar Dust, ed. L. J. Allamondola & A. G. G. M. Tielens (Dordrecht: Kluwer), 431
McKee, C. F., Hollenbach, D. J., Seab, C. G., & Tielens, A. G. G. M. 1987, ApJ, 318, 674
McKee, C. F., & Ostriker, J. P. 1977, ApJ, 218, 148
Nagel, K., & Fechtig, H. 1980, Planet. Space. Sci., 28, 567
Orphal, D. L. 1977, in Impact and Explosion Cratering, ed. D. J. Roddy, R. O. Pepin, & R. B. Merrill (New York: Pergamon), 907
Raymond, J. 1992, private communication
Rinehart, J. S., & Pearson, J. 1954, Behavior of Metals under Impulsive Loading (Cleveland: Am. Soc. Metals)
Routly, P. M., & Spitzer, L. 1952, ApJ, 115, 227
Rudolph, V. 1969, Z. Nat., 24A, 326
Seab, C. G., & Shull, J. M. 1983, ApJ, 275, 652
Sembach, K. R., & Savage, B. D. 1996, ApJ, 457, 211
Swegle, J. W., & Grady, D. E. 1986, J. Appl. Phys. B, 58, 692
Thomsen, J. M., Austin, M. G., Ruhl, S. F., Schultz, P. H., & Orphal, D. L. 1979, Proc. Lunar Planet. Sci. Conf. 11th, 2741
Tielens, A. G. G. M. 1989, in Interstellar Dust, ed. L. J. Allamandola & A. G. G. M. Tielens (Dordrecht: Kluwer), 239
———. 1990, in Carbon in the Galaxy, ed. J. C. Tarter, S. Chang, & D. De Frees (NASA Conf. Publ. 3061), 59
———. 1993, in Dust and Chemistry in Astronomy, ed. T. J. Millar & D. A. Williams (Bristol: Institute of Physics Publishing), 103
Tielens, A. G. G. M., McKee, C. F., Seab, C. G., & Hollenbach, D. J. 1994, ApJ, 431, 321
Trulio, J. G. 1977, in Impact and Explosion Cratering, ed. D. J. Roddy, R. O. Pepin, & R. B. Merrill (New York: Pergamon), 1301
Vedder, J. F. 1971, Earth Planet. Sci. Lett., 11, 291
———. 1976, Moon, 15, 31
Zeldovich, Y. B., & Raizer, Y. P. 1966, Physics of Shock Waves and High Temperature Phenomenae (New York: Academic)